CERN/LHCC 2003–003
LHCC–G–023

LHCb 2003–006
LHCC

23 January 2003

Status of the LHCb Detector Reoptimization

The LHCb Collaboration

Contents

1 Introduction

For the study of CP violation beyond the framework of the Standard Model, a high statistics sample of reconstructed B mesons, in particular B_s^0 mesons, from various decay modes is essential. To achieve this goal, LHCb must have a high track reconstruction efficiency, pion–kaon separation capability from few GeV/c to $\sim$100 GeV/c, a very good proper-time resolution of $\sim$40 fs and high trigger efficiencies, not only for the final states including leptons but also for those with hadrons alone. It was shown in the Technical Proposal (TP) [1] that the LHCb detector fulfils these requirements.

By the time of the Outer Tracker Technical Design Report [2], the LHCb detector had evolved into the layout shown schematically in Fig. 1 (a). The spectrometer consists of the Vertex Locator (VELO), two Ring Imaging Cherenkov Counters (RICH-1 and RICH-2), the Calorimeter system and the Muon system. A total of nine tracking stations (T1–T9) were used to reconstruct charged tracks which were then linked to tracks reconstructed in the VELO. A shielding plate protected the photon detectors of RICH-1 from the fringe field of the magnet.

As the engineering design of the subsystems matured, their material budget increased, particularly for the VELO and tracking stations. The material up to RICH-2 corresponded to 40% of X_0 (10% of λ_{I}) at the time of the TP, and had increased to 60% (20%) at the time of the Outer Tracker TDR, where X_0 (λ_{I}) is the radiation (nuclear interaction) length. Detector material with a large radiation length deteriorates the detection capability of $e^{\pm}$ and photons, increases the multiple scattering of charged particles, and increases occupancies of the tracking stations. With increased nuclear interaction length, more kaons and pions interact before reaching the last station of the tracking system. The number of reconstructed B mesons therefore decreases, even if the efficiency of the tracking algorithm is maintained high for those tracks that traverse the full spectrometer [3]. For this reason, the detector has been reoptimized to reduce the material budget to the level of the TP.

A second aspect of the reoptimization concerns the LHCb trigger. The trigger is designed to distinguish minimum-bias events from events with B mesons by requiring the presence of particles with a large transverse momentum (p_{T}) and the existence of secondary vertices. Events are first triggered by requiring at least one lepton or hadron with a p_{T} exceeding $\sim$1 to 3 GeV/c (Level-0) reducing the event rate to 1 MHz. At the next level (Level-1) two-track vertices are formed using large-impact-parameter tracks reconstructed in the VELO, which reduces the event rate to 40 kHz. Accepted events are read out for further on-line processing and selection. The Level-1 trigger has been modified to increase its efficiency and robustness, by adding p_{T} information to tracks with a large impact parameter.

Figure 1 (b) shows a schematic layout of the reoptimized detector.

1.1 Reduction of material

At the time of the TP the beam pipe was foreseen to be made of aluminium; it was changed to Be/Al alloy for the Outer Tracker TDR. Now the first (25 mrad cone) section of the beam pipe will be made from pure beryllium. The second section

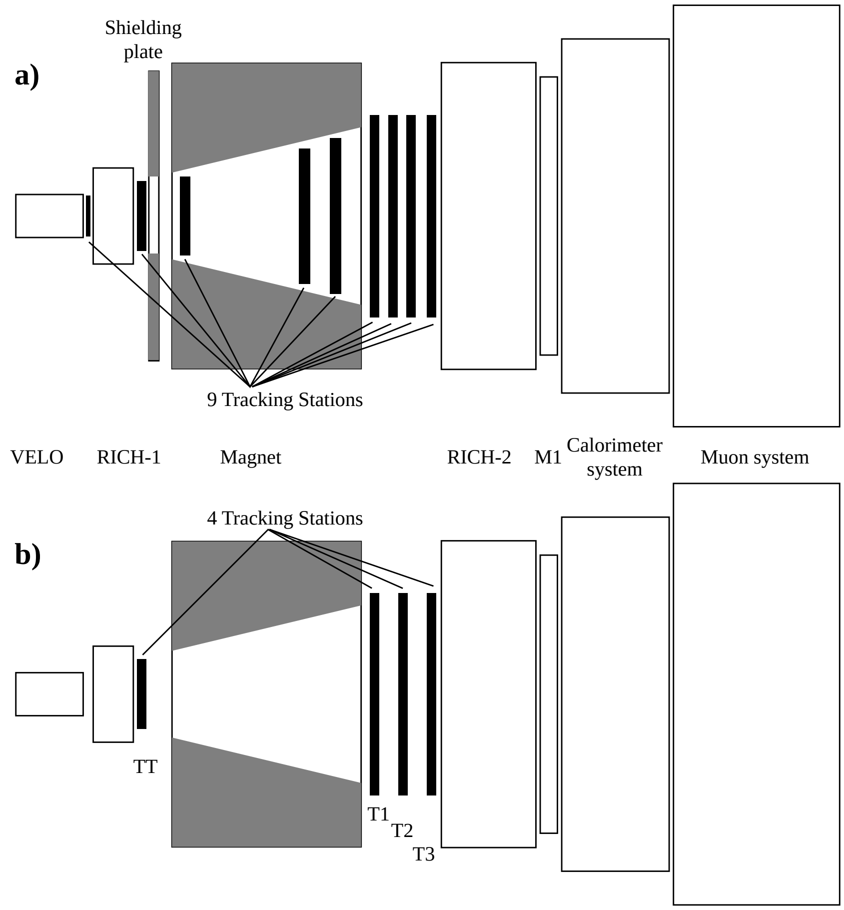

Figure 1: A schematic view of the LHCb detector: (a) before the reoptimization and (b) after the reoptimization.

(10 mrad cone) is still Be/Al alloy, however it may also be changed to beryllium, depending on the price.

The material budget of the VELO and RICH-1 has been reduced by minor modifications and improvements in their design. For the VELO, the thickness of the silicon sensors has been reduced from 300 to 220 μm, and the number of stations from 25 to 21, compared to the VELO TDR [4]. Figure 2 shows the number of VELO stations traversed by the tracks within the LHCb acceptance. It demonstrates that the number of tracks with three or four hit stations are practically unchanged by reducing the number of stations. The number of tracks with a large number of hit stations (more than $\sim$10) is reduced for the layout with 21 stations; however, such a large number of stations is not needed for track reconstruction. Therefore, neither the impact parameter resolution nor the acceptance of the VELO are affected by the design modification. Compared to the RICH TDR [5], the material of the RICH-1 mirror has been changed from glass to carbon-composite material and the mirror supports have been moved outside the acceptance.

For the Outer Tracker, it was found to be very difficult to reduce material below

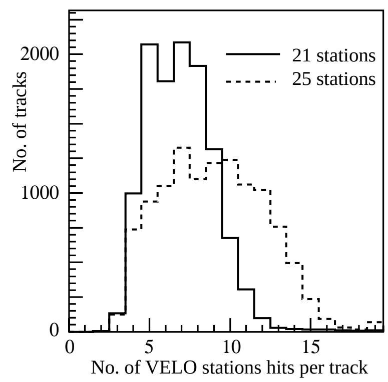

Figure 2: The number of VELO stations traversed by tracks in the LHCb acceptance for the VELO with 25 stations (as in the TDR, dashed line) and with 21 stations after reoptimization (solid line).

a level of 3% of X_0 (1.2% of λ_{I}) per station. A reduction in the number of tracking stations was therefore considered. As described in the Outer Tracker TDR [2], occupancies of the tracking stations in the magnet were high due to low momentum particles (from secondary interactions) trapped in the magnetic field. In the case of electrons, if the emission of photons occurs while the particle is in the magnetic field, recovery of the photons using the Calorimeter system behind the magnet is difficult [6]. These problems have been avoided by removing the stations in the magnet. The number of tracking stations behind the magnet has been reduced from four to three (T1, T2 and T3), which are now of identical construction. Since each station has eight measurement layers for the straw Outer Tracker part and four layers for the silicon Inner Tracker part, three stations are found to be sufficient. The pattern recognition has been adapted to this layout, and now relies mainly on matching tracks found in the VELO to the hits in T1–T3.

An additional station, the Trigger Tracker (TT), is placed in front of the magnet just behind RICH-1. By matching the track segments found in stations T1–T3 to the hits in TT, pions from $\mathrm{K^0_S}$ decaying outside the VELO volume but upstream of TT can be reconstructed. Additionally, in combination with the VELO, TT allows the reconstruction of those low momentum tracks (mostly below $3\,\mathrm{GeV}/c$) that do not reach T1–T3.

While the design of the T1–T3 stations remains unchanged from that described in the Outer and Inner Tracker TDRs [2, 8], the design of TT is based entirely on silicon microstrip detectors. This is due to a requirement from the Level-1 trigger as described in the next subsection.

After this reoptimization, the material budget in front of RICH-2 is now back to the level of 40% of X_0 and 12% of λ_{I}.

As a final step, the possibility of reducing the material in the first Muon station (M1) has been examined. In the design presented in the Muon System TDR [7], M1 contained material corresponding to 30% of X_0, in front of the calorimeter system, affecting the reconstruction of γ and π^0. This has been reduced to below 18% of

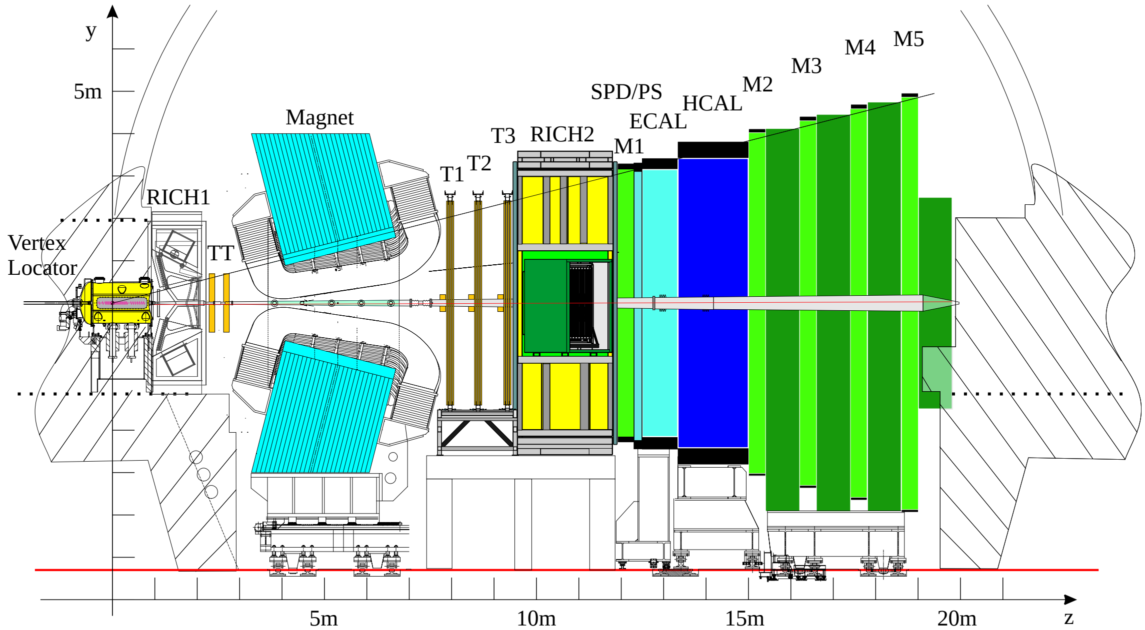

Figure 3: Optimized LHCb detector layout, showing the Vertex Locator (VELO), the two RICH counters, the four tracking stations TT and T1–T3, the Scintillating Pad Detector (SPD), Preshower (PS), Electromagnetic (ECAL) and Hadronic (HCAL) Calorimeters, and the five muon stations M1–M5.

X_0 without compromising the Muon trigger performance, by reducing the number of layers of wire chambers from four to two.

1.2 Detector change for the Level-1 trigger

In addition to the successful attempt to reduce the material budget of the detector, a strong effort has been made to improve the trigger. It was realised that the robustness and efficiency of the Level-1 trigger could be significantly improved by not only using information from the VELO, as done in the TP, but also adding p_{T} information to tracks with a large impact parameter. This is achieved by associating the high-p_{T} calorimeter clusters and muons obtained at Level-0 to the tracks found in the VELO [9]. Implementation of this algorithm requires no modification to the detector.

A complementary approach that is more efficient for hadrons is to extrapolate the tracks with a large impact parameter to TT, and to determine p_{T} by introducing a small magnetic field in between the VELO and TT. This B field is introduced by removing the shielding plate that was foreseen to be placed in front of the magnet. The RICH-1 design is modified to incorporate a second flat mirror and magnetic shielding boxes around the photon detectors. It is found that the trigger performance can be improved if TT is constructed entirely of silicon detectors [10], due to their better spatial resolution and granularity compared to straws. In addition the four layers of TT are split into two pairs of layers separated by 30 cm, to measure the bending angle of tracks in the fringe field of the magnet between the VELO and TT.

Figure 3 shows a side view of the reoptimized LHCb detector placed in the experimental area.

1.3 Scope of the document

This document reports the status of the work going on to reoptimize the LHCb detector. It shows the updated performance of track reconstruction, particle identification and the triggering capability, which are all found to be satisfactory. Preliminary event yields for several decay channels are shown to be comparable to those shown in the TP, confirming that the physics goals of the TP can be achieved.

Detailed engineering designs of RICH-1 and the TT station are still in progress and will be given in a document (the Reoptimization TDR) to be submitted later. Results on the physics performance are still preliminary and will be finalized, together with the analysis of further channels, for the TDR. However, the current status is already sufficient to demonstrate the validity of the reoptimized LHCb detector layout.

2 Event Generation

Minimum bias proton-proton interactions at $\sqrt{s} = 14$ TeV are generated using the PYTHIA 6.2 program [11], including hard QCD processes, single diffraction and double diffraction; elastic scattering never produces tracks in the detector. Samples of $b\bar{b}$ events are obtained by selecting events with at least one b- or $\bar{b}$-hadron in a large minimum-bias data-set (PYTHIA option `MSEL=2`). The total inelastic and $b\bar{b}$ production cross-sections obtained in this mode are 79.2 mb and 633 μb respectively. In the following, we explain how some of the PYTHIA parameters have been tuned based on the available data.

Several parton-parton interactions can occur in a single proton-proton collision. In PYTHIA, the average number of such interactions, and hence the average particle multiplicity in a proton-proton collision, is controlled by a parameter $p_{\mathrm{T}}^{\mathrm{min}}$ that represents the minimum transverse momentum of the parton-parton interaction. Different multiple parton-parton interaction models are available in PYTHIA, which mainly affect the shape of the particle multiplicity distribution. One of these models, called Model 3 in PYTHIA (`MSTP(82)=3`) and originally developed [12] to reproduce the UA5 data, assumes a varying impact parameter between the two colliding protons that are described with Gaussian distributions. Figure 4 shows that the UA5 data [13] indeed favour such a model over another PYTHIA model (Model 1, i.e. `MSTP(83)=1`) which assumes that all the proton-proton collisions have a fixed impact parameter. Studies performed by the CDF collaboration [14, 15] also conclude that a varying impact parameter model is preferred to describe the minimum-bias events and the underlying particles in $b\bar{b}$ events produced in $p\bar{p}$ collisions at $\sqrt{s} = 1.8$ TeV. Model 1 is the default in PYTHIA and was used for the performance studies reported

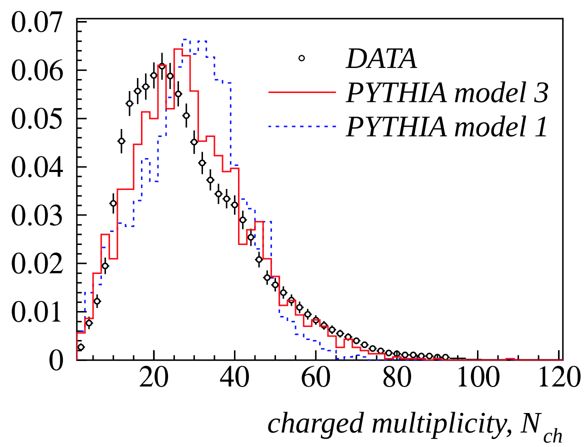

Figure 4: Charged multiplicity distribution for non single-diffractive events in $p\bar{p}$ collisions at $\sqrt{s} = 546$ GeV as measured by UA5 [13], compared with PYTHIA predictions using the CTEQ4L parton distribution functions and either Model 1 (solid) or 3 (dashed) for multiple interactions. In each case the $p_{\mathrm{T}}^{\mathrm{min}}$ parameter has been tuned to reproduce the mean multiplicity measured in the data.

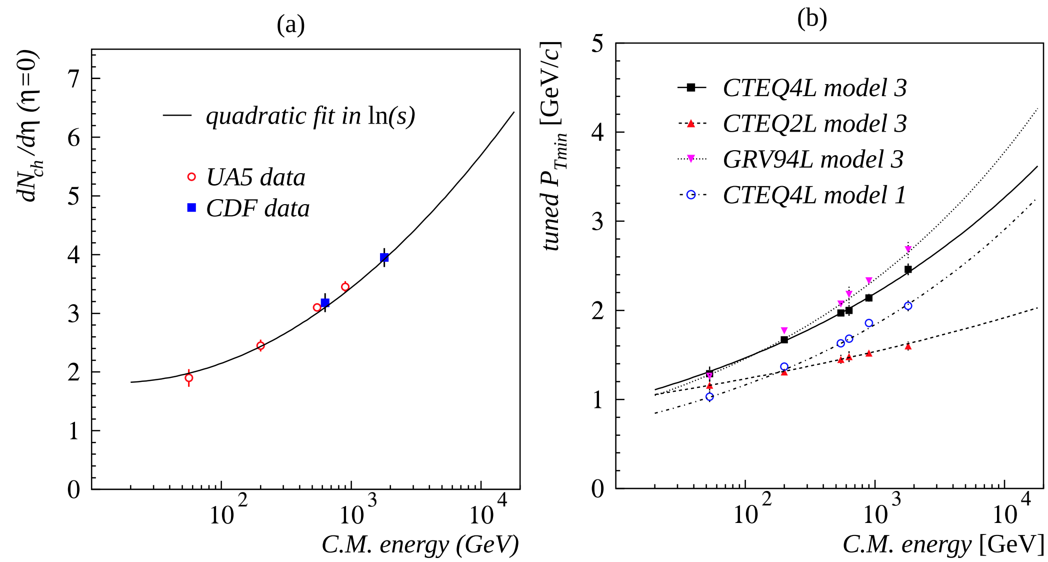

Figure 5: (a) Average charged multiplicity at $\eta = 0$ measured at different energies by UA5 and CDF. (b) Corresponding values of $p_{\rm T}^{\rm min}$ which allow PYTHIA to reproduce these data, using different multiple interaction models or parton distribution functions. Details can be found elsewhere [16].

in the Technical Proposal; however, all simulation studies for subsequent Technical Design Reports have been performed with Model 3.

In Fig. 5 (a) the densities of charged particles at $\eta = 0$, where η is the pseudorapidity, are plotted for non single-diffractive events measured at six different center-of-mass energies ranging from 50 to 1800 GeV [17, 18]. The figure also shows the result of a quadratic fit in $\ln(s)$ [18] to the data. From the extrapolation of the fit, we obtain

$$(dN_{\rm ch}/d\eta)_{\eta=0}^{\rm direct\ fit} = 6.11 \pm 0.29 \quad \text{at } \sqrt{s} = 14 \text{ TeV}\,, \tag{1}$$

where the quoted error is due to the statistical uncertainty of the fit.

Using PYTHIA Model 3, the value of the $p_{\rm T}^{\rm min}$ parameter has been tuned [16] so as to reproduce those measured charged particle densities at $\eta = 0$ for different parametrizations of the structure functions. The tuned $p_{\rm T}^{\rm min}$ values, displayed in Fig. 5 (b), show an energy dependence which is well described by a power law, as advocated in recent PYTHIA versions. Although the values of $p_{\rm T}^{\rm min}$ themselves strongly depend on the assumed set of structure functions, the predicted charged particle density at $\eta = 0$ obtained at the LHC energy using the extrapolated values of $p_{\rm T}^{\rm min}$ depend only weakly on the choice of the structure functions. Choosing the CTEQ4L parton distribution functions together with Model 3, as PYTHIA settings for the LHCb simulation study, an extrapolated value of

$$p_{\rm T}^{\rm min} = 3.47 \pm 0.17 \text{ GeV}/c \quad \text{at } \sqrt{s} = 14 \text{ TeV} \tag{2}$$

is obtained. A central value of 3.47 GeV/c is therefore used as default to generate

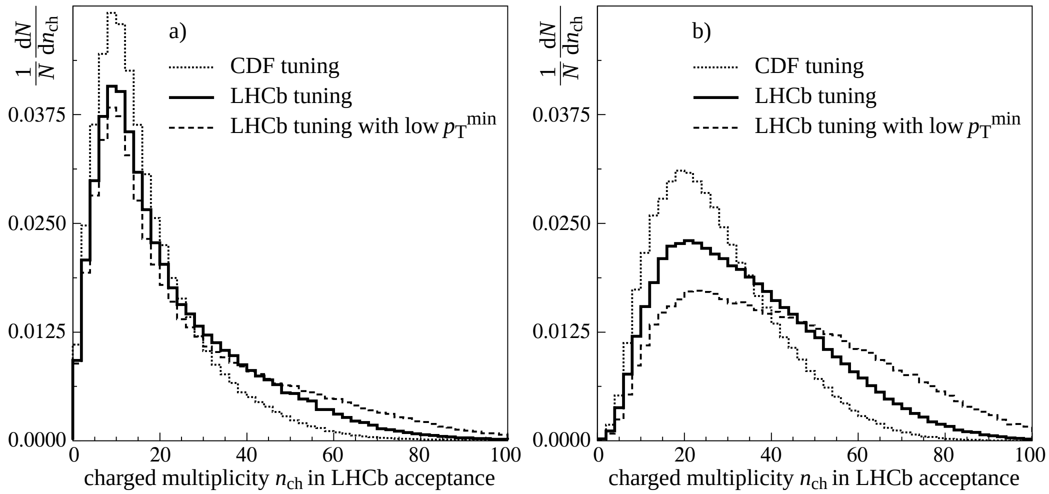

Figure 6: Charged multiplicity distributions in the LHCb acceptance ($1.8 < \eta < 4.9$) for (a) minimum-bias collisions and (b) collisions producing b-hadrons, as predicted by PYTHIA 6.2 with `MSEL=1` (hard collisions) and different settings for multiple parton-parton interactions. The plain histograms are obtained with the nominal LHCb settings, the dashed histograms with modified LHCb settings where $p_T^{\min}$ of Eq. (2) is lowered by three times its uncertainty, and the dotted histograms with a recent tuning from CDF [19]. Decay products of K_S^0 mesons and Λ baryons are not counted.

collisions in LHCb, which leads to

$$(dN_{\rm ch}/d\eta)_{\eta=0}^{p_{\rm T}\ \rm fit} = 6.30 \pm 0.42 \quad \text{at } \sqrt{s} = 14 \text{ TeV}\,. \tag{3}$$

This is in good agreement with Eq. (1), the direct fit of Fig. 5 (a), supporting the validity of the PYTHIA prediction at the LHC energy.

Contrary to Model 1, a model for multiple parton-parton interactions with varying impact parameter results in significantly different multiplicities for minimum-bias and $b\bar{b}$ events. This is illustrated in Fig. 6, where various predictions are shown for the distribution of the number of charged particles produced in hard pp collisions at LHC energy in the pseudo-rapidity region $1.8 < \eta < 4.9$, corresponding roughly to the LHCb acceptance. The mean charged multiplicity is larger in $b\bar{b}$ events than in minimum-bias events. With the nominal LHCb settings for PYTHIA (i.e. Model 3 tuned as explained above) these averages are 33.9 and 21.3 respectively; they increase by 26% and 19% if the value of $p_T^{\min}$ from Eq. (2) is lowered by three times its uncertainty.

The CDF collaboration has recently published [15] their tuning of PYTHIA 5.7 which reproduces best the soft and hard interactions they observe in $p\bar{p}$ collisions at $\sqrt{s} = 630$ and 1800 GeV; it involves Model 4 for multiple parton-parton interactions, a variant of Model 3 with a double-Gaussian parametrization of the matter distributions of the colliding hadrons. Using an updated version of this tuning [19], valid

Table 1: Average probabilities F_i to produce i visible pp collisions and average number $\sum_{i=1}^{\infty} iF_i$ of such collisions in bunch crossings producing at least one visible collision. This table effectively gives the pile-up distribution and average in the generated minimum-bias sample (first line) and $\mathrm{b\bar{b}}$ sample (second line). Absolute uncertainties from MC statistics are approximately 0.001.

	F_1	F_2	F_3	F_4	F_5	$\sum_{i=1}^{\infty} iF_i$
All bunch crossings	79.9%	17.2%	2.6%	0.3%	0.0%	1.234
Crossings producing b-hadrons	64.9%	27.8%	6.2%	1.0%	0.1%	1.420

for PYTHIA 6.2 and claimed to reproduce minimum-bias data and the "underlying event" in hard scattering processes at the two Tevatron energies, the average multiplicities predicted in LHCb would be approximately 20% lower than those obtained with the nominal LHCb settings.

Several inelastic proton-proton collisions may occur in the same bunch crossing. This "pile-up" phenomenon is simulated assuming that the number of pp interactions in one bunch crossing follows a Poisson distribution with mean given by $L\sigma_{\mathrm{inel}}/\nu$, where L is the instantaneous luminosity, σ_{inel} is the inelastic cross section taken to be 80 mb, and $\nu = 30$ MHz is the average non-empty bunch crossing frequency at the LHCb interaction point. The luminosity L is assumed to decrease exponentially with a 10-hour lifetime in the course of 7-hour fills, with an average value of 2×10^{32} cm^{-2}s^{-1} (implying a maximum value of $\sim 2.8 \times 10^{32}$ cm^{-2}s^{-1} at start of fill). In practice, only "visible" collisions contribute to the pile-up; we define such collisions as the ones producing at least two charged particles reconstructible as long tracks in the detector (according to the definition of Section 4.1), corresponding to $(79.1 \pm 0.2)\%$ of σ_{inel}. Pile-up characteristics, averaged over a fill and considered for visible collisions only, are given in Table 1 for minimum-bias and $\mathrm{b\bar{b}}$ events.

The decay of all unstable particles is performed with the QQ program [20], originally developed by the CLEO collaboration, using a decay table from CDF which includes also $\mathrm{B_s^0}$ and b-baryon decays.

3 Software Framework

The software chain used for the performance study consists of the following components:

1. Event generation;
2. Tracking particles through the detector material;
3. Simulation of the detector response;
4. Reconstruction of the event;
5. Physics analysis.

The first step of event generation was explained in the previous section. Once particles are generated, they are tracked through the detector material and surrounding environment using the GEANT3 package [21]. The geometry of the LHCb detector is described in detail, including passive material such as frames and supports. Particles produced in the interactions are traced to as low as $E = 10$ MeV for hadrons, 1 MeV for electrons and photons. By generating some data with a factor 10 lower threshold values and studying the response of the detector, it has been confirmed that those values are appropriate [22].

In the simulation program the entrance and exit points of a particle traversing a sensitive detection layer are registered as well as the energy loss in that layer and the time-of-flight of the particle with respect to the interaction time. The effect of tracks from the two preceeding and one following bunch crossings are properly taken into account according to the sensitivities of the sub-systems. This is referred to as "spill-over".

In the Muon system, the number of hits generated by charged particles is rather low, and the neutron-induced background thus becomes relevant. Since the time structure of this background is very different from that due to the charged particles, special studies have been made to find a suitable parametrization to include the effect in the response of the Muon system [23].

Up to this step, the software is still written in FORTRAN. The rest of the software has now been integrated into the GAUDI framework [24], based on object-oriented technology. This process was completed in July 2002.

Once the particles have been tracked through the LHCb detector, the details of the detector response are simulated. Detection efficiencies and resolutions of the individual sub-systems are adjusted using results from beam tests of prototypes. Electronics noise and cross-talk are also included.

The simulated detector response is then used for event reconstruction. The charged particle trajectories are reconstructed using the VELO and the tracking system, comprising the TT station before the magnet and the T1–T3 stations after the magnet. The T1–T3 stations are composed of Inner Tracker (IT) and Outer Tracker (OT) parts. The search for tracks in the VELO is performed first; to avoid spending a disproportionate amount of time on the very highest multiplicity events, the rest of the tracking algorithms were not applied if more than 200 tracks were found in the VELO. This occured for 2.3% of the generated events; it has been checked that they would not affect the final physics yields significantly, as they are mostly rejected by the trigger.

Electromagnetic and hadronic clusters are reconstructed using the Calorimeter system, and muons are reconstructed using the Muon system. Together with the reconstructed track parameters, Cherenkov photons detected as photoelectrons in the RICH system are used to calculate the probabilities that each track is of a given charged-particle type: e, μ, π, K or p. The data are processed as if they were from real events, without reference to any information from the Monte Carlo truth. The truth information is used only when the performance of the reconstruction is examined. The output of the event reconstruction is written as ROOT–IO [25] data files for physics analysis.

In the physics analysis, primary and secondary vertices are determined using the charged particle tracks. Photons and electrons are identified by combining the information of the reconstructed electromagnetic clusters and tracks. The particle identification information from the RICH system is combined with that from the Muon and Calorimeter systems to improve the performance. Tools have been implemented to ease the analysis of B meson final-state reconstruction.

3.1 Simulation of tracking detector response

To demonstrate the level of detail of the detector simulation, the part related to the tracking is described here at some length. The digitization program simulates the response to each registered GEANT hit in a sensitive detector layer. For the tracking detectors the response simulation can be classified into two categories: silicon detector response (VELO, TT and IT) [26] and straw detector response (OT) [27].

3.1.1 Silicon detector response

In the silicon strip detectors the number of primary electrons corresponding to the energy loss are distributed along the trajectory inside the silicon material. The trajectory is subdivided into parts, in each of which the number of electrons is sampled from a Landau distribution. Subsequently, the electron signals of each part are collected on the readout strips by applying a charge sharing function, which is tuned to describe test-beam data. For each strip a noise signal is added according to a Gaussian distribution corresponding to a signal-to-noise ratio of 15 (VELO) or 12 (TT and IT). A 5% (VELO) and 10% (TT/IT) cross-talk between neighbouring strips is also implemented. A strip causes a hit if the signal surpasses a threshold corresponding to 3 sigma of the noise. The effective efficiency for a layer to observe a traversing particle is >99% (VELO), 96% (TT) and 96.5% (IT). The reasons for the slightly lower TT/IT efficiencies are the assumption that 1% of the silicon strips are inoperative, the presence of small insensitive regions between the silicon sensors of the TT/IT detector planes (such as guard rings), and the slightly reduced efficiency due to the imperfect charge collection in the region between two strips for the large

TT/IT strip pitch [8].

The analog front-end pulse shape has a remaining amplitude of approximately 30% for VELO and IT, and 50% for TT, after 25 ns. This is taken into account by applying the same procedure as mentioned above to all hits caused by the previous bunch-bunch collisions at −25 ns and −50 ns after reducing the amplitudes accordingly.

3.1.2 Straw detector response

In the straw detectors the path length of a traversing track in each straw is calculated, as is its distance of closest approach to the wire. A hit efficiency is assigned based on the calculated trajectory length l and effective primary ionization density ρ, using the parametrization [2]:

$$\eta(l) = \eta_0 \, (1 - e^{-\rho l})$$

where $\eta_0 = 0.99$ and $\rho = 1.47\,\mathrm{mm}^{-1}$ have been tuned to reproduce OT test-beam results [27], leading to an integrated cell efficiency of 97%. If a hit is registered, a detector response time is generated according to:

$$t_{\mathrm{TDC}} = t_{\mathrm{bunch}} + t_{\mathrm{tof}} + t_{\mathrm{drift}} + t_{\mathrm{delay}}$$

where t_{bunch} is the bunch time $(-50,\,-25,\,0,\,25)$ ns, t_{tof} is the time-of-flight of the track as it passes through the straw, t_{drift} is the drift time in the cell and t_{delay} is the additional time delay due to signal propagation along the wire. A measurement resolution of 200 μm, again based on test-beam measurements [2], is implemented by smearing t_{drift} accordingly.

Since the front-end readout works with a 50 ns sensitive time gate, a hit is only registered if it falls in a time window $t_0 < t_{\mathrm{TDC}} < t_0 + 50$ ns. The value t_0 is calibrated for each station as the rising edge of the time spectrum of all hits from the bunch at $t = 0$. In case two or more tracks pass through a single straw only the one with the earliest t_{TDC} is registered, for the others the straw is inefficient. Finally, cross-talk between straws is implemented such that in 5% of the cases a signal in a neighbouring straw is generated (with identical t_{TDC}).

The overall efficiency to produce at least one hit in a double layer depends on the momentum of a track;[1] for $p > 2\,\mathrm{GeV}/c$ the overall efficiency is 98%. The measurement resolution also depends on the track momentum,[2] however for tracks with $p > 2\,\mathrm{GeV}/c$ it is close to 200 μm.

[1]Due to the fact that very low momentum tracks (often secondaries) have significantly longer time-of-flight, the digitization time t_{TDC} can occasionally fall outside the sensitive time gate, resulting in inefficiency.

[2]The longer time-of-flight for low momentum tracks leads to a biased drift time measurement after t_0 subtraction, which results in a worse resolution for very low momentum tracks.

4 Track Reconstruction

4.1 Track pattern recognition

At the time of the Technical Proposal a full pattern recognition program was not yet in place. Only general requirements on tracks, such as having hits both upstream and downstream of the magnet, were implemented. Such tracks were labelled as "physics tracks" and were assumed to be found with full efficiency. No "ghost" tracks, i.e. tracks not associated to a single Monte Carlo particle, were generated.

For the Outer Tracker TDR, pattern recognition was implemented for the tracker set-up shown in Fig. 1 (a). Track segments were found in four seeding stations, T6–T9, and were followed in the upstream direction through the magnet up to T1 where they were finally matched to VELO tracks, which were assumed to be found with 100% efficiency. In this procedure the track finding efficiency was found to be 91% for a ghost rate of 16% [2]. The dominant source of ghost tracks was the seeding procedure, while track following reduced the ghost rate at the cost of an additional 4% efficiency loss (compared to the efficiency of 95% that was obtained for the seeding alone).

For the reoptimized LHCb set-up shown in Fig. 1 (b), alternative algorithms suitable for the new tracking layout have been developed. Existing algorithms have also been adapted to the new set-up.

4.1.1 Track types and tracking strategy

The following track types are defined, related to their trajectories inside the spectrometer, as illustrated in Fig. 7:

1. **Long tracks** which traverse the full tracking detector set-up, generating hits in the VELO as well as in the T1–T3 stations. Long tracks are used in all physics analyses.

2. **V→TT tracks** leaving hits in the VELO and TT station only. These are in general lower momentum tracks which do not traverse the magnet. They pass through the RICH-1 detector and may generate Cherenkov photons. They are therefore useful to help understand photon backgrounds in the particle identification algorithm of the RICH. In addition specific final states such as D^* decays, as well as the kaon tagging procedure, profit from the detection of low momentum particles.

3. **T→TT tracks** leaving hits in the TT and T stations only. The most relevant cases are the decay products of K^0_S and Λ that decay outside the VELO acceptance.[3]

4. **VELO tracks** leaving hits inside the VELO only. These are typically large angle or backward tracks, used in the primary vertex reconstruction.

[3] In $B^0 \to J/\psi K^0_S$ events, about 25% of the K^0_S decays are expected to occur in the VELO, 50% outside the VELO acceptance but before the TT station, and 25% downstream of TT.

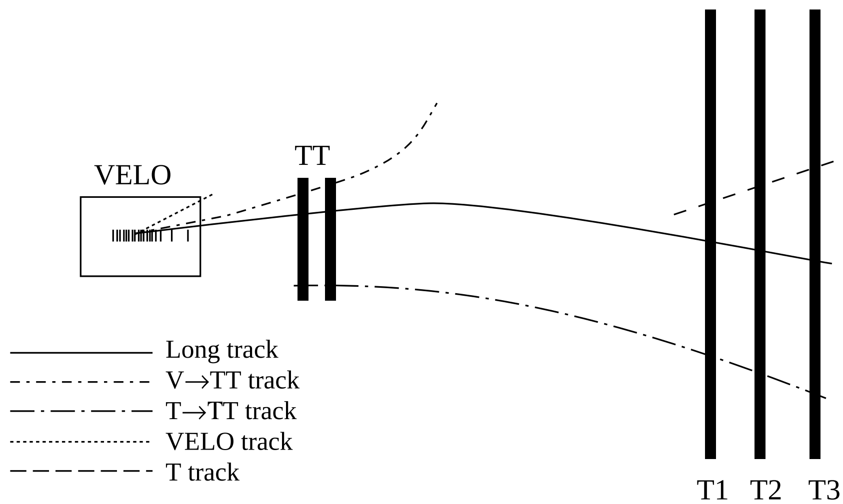

Figure 7: A schematic illustration of the various track types: long tracks, V→TT tracks, T→TT tracks, VELO tracks and T tracks.

5. **T tracks** only leaving hits in the T1–T3 stations. Typically these are secondaries which are of use for the RICH-2 background subtraction.

For the reconstruction of B mesons with good mass and proper-time resolution, the long tracks are most relevant. The main aim of the reoptimization of the detector has been to improve the overall reconstruction efficiency for the long tracks. By reducing the material, more tracks reach the last tracking station without interacting. The algorithms also profit from the overall reduction of secondary particles. The particular case of the reconstruction of T→TT tracks is more difficult in the reoptimized set-up.

The algorithms can be broadly categorized into those that work in the "downstream" direction and those that work in the "upstream" direction. The downstream approach starts with a search for straight line track segments in the VELO ("VELO tracking"). Continuations of these VELO tracks are then looked for directly in stations T1–T3 ("forward tracking") or only up to the TT station ("V→TT tracking"). The upstream approach starts with track seeding in stations T1–T3 ("seeding") which are then either matched to the straight line segments in the VELO ("matching") or confirmed in the TT station ("T→TT tracking").

It should be noted that "long" tracks can be found either in the forward pattern recognition method or in the matching method. Combination of the two provides robustness and flexibility. The individual algorithms are summarized in the next subsection.

4.1.2 Pattern recognition algorithms

VELO tracking: In the VELO tracking procedure a search is made for straight-line segments inside the VELO detector using the r and ϕ clusters reconstructed from silicon strip hits. Candidate track seeds are created using triplets of hits in the rz plane. Space points are built by combining these seeds with the ϕ clusters in the same stations. A triplet is accepted as a 3D track-seed if the middle point of the triplet lies within $2\,\sigma$ from a straight-line interpolation between the two other points. If a track-seed is found, the search is extended to the next station using a wider cut. This continues until the extrapolation runs out of the VELO acceptance. To allow for detector inefficiencies the algorithm may skip up to two stations before a given track search is aborted.

A cleaning procedure is applied to avoid clones. If complete r or ϕ projections are identical for two track candidates, or if they share more then 30% of their hits, the shorter of the two is removed; in case they have equal length, the one with the lowest χ^2 is kept.

Seeding: Track seeding is a standalone algorithm to find track segments in the T1–T3 stations [28]. It exploits the fact that those stations lie in a region of low magnetic field, so that tracks are close to straight lines. Track seeding first looks for track candidates in the xz plane by considering "roads" of hits of the x measurement planes; this is done first with a linear parametrization and then refined with a parabolic parametrization, with tighter cuts around the road. The 2D track candidates are confirmed as 3D tracks in a second step using the hits of the stereo measurement planes. A likelihood is built, based on the fitted trajectory, for observing the number of hits seen after traversing the given number of measurement planes. It is based on the expected detector efficiencies and takes into account insensitive areas along the trajectory. A cut is applied on the likelihood to reject ghost tracks.

Forward tracking: Forward tracking searches for track continuations of VELO tracks in the T1–T3 stations [29]. Extrapolation of VELO tracks across the magnet region is inaccurate as long as the track momentum is not known. The forward tracking method is based on the idea that the momentum can be determined as soon as an x-measurement downstream of the magnet is added to the track. Thus, for a given combination of a VELO track and a single hit in one of the T1–T3 stations, all other expected hit positions along the trajectory can be predicted. To make this procedure fast, the trajectories in the T1–T3 station region are parametrized by polynomials of order 3 (2) in the xz (yz) plane. A parameterization based on a reference sample of events allows these trajectory parameters (the coefficients of the polynomials) to be computed as function of the parameters of the VELO track segment $(x, y, dx/dz, dy/dz)$ and the position at a reference plane in T3.

If the assumed combination of VELO track and hit in the T1–T3 stations is correct, the additional hits along the trajectory are picked up by a fast histogramming method and the track candidate is finally confirmed using a likelihood method similar to that of the seeding procedure above. Finally TT hits are added to the track, to provide the optimal measurement of the trajectory.

Matching: The matching algorithm combines already found track segments of the VELO tracking and seeding algorithms [30]. The T track is extrapolated in the upstream direction and a prediction at the last VELO station is made. As is the case for the forward tracking, the transport across the magnet requires an estimate of the track momentum. Here, the so-called "p_{T}-kick" method is used. Assuming that a reconstructed T track (i.e. position (x, y) and slope $(dx/dz, dy/dz)$ at station T3) originates from the nominal vertex (0,0,0) provides a momentum estimate with an average resolution of 1%. The matching procedure compares the positions and slopes of the VELO tracks and extrapolated seed tracks at the same position, and applies a χ^2 criterion to select correct matches.

V→TT tracking: The V→TT tracking algorithm reconstructs tracks which pass through the VELO and TT station but do not reach the T1–T3 stations. The algorithm uses all VELO track segments which have not yet been assigned to long tracks and extrapolates them as straight lines in the yz-plane into TT. It then considers the hits compatible with this extrapolation on all silicon wafers and requires that at least 3 out of 4 layers match in the xz plane to the VELO segment, using the same momentum parameter. The track is then refitted with the full Kalman fit through all clusters. The candidate is kept if the required criterion of $\chi^2/\mathrm{NDF} < 5$ is fulfilled.

T→TT tracking: The T→TT algorithm reconstructs tracks which leave no (or insufficient) hits in the VELO, but do traverse the TT and T1–T3 regions. It uses unassigned T tracks and extrapolates them upstream across the magnet into the TT station, using a similar p_{T}-kick method as the matching algorithm. The momentum estimate required as input for this extrapolation is again obtained by assuming that the reconstructed T track originates from the origin (0,0,0). Even though the pions produced in a $\mathrm{K^0_S}$ decay do no strictly point back to this origin the momentum estimate is found to be correct within 2% on average. A clustering algorithm then assigns candidate TT hits to the track and a full Kalman refit is applied.

4.1.3 Performance

The pattern recognition performance is evaluated in terms of efficiencies and ghost rates. The efficiencies are normalized to a sample of "reconstructible" particles. To be considered reconstructible, the requirements for each track type are as follows: for VELO tracks the particle must give at least $3\,r$ and $3\,\phi$ hits; for T tracks the particle must give at least $1\,x$ and 1 stereo hit in each station T1–T3; for long tracks the particle must be reconstructible as both a VELO and T track; for V→TT tracks the particle must be reconstructible as a VELO track and give at least 3 hits in TT; for T→TT tracks the particle must be reconstructible as a T track and give at least 1 hit in TT.

To be considered as "successfully reconstructed" a VELO or T track must have at least 70% of its hits originating from a single Monte Carlo particle, a V→TT or a T→TT track must have in addition a correct TT hit assigned, and a long track must have both correctly found VELO and T track segments. The efficiency is defined as the fraction of reconstructible particles that are successfully reconstructed, and the ghost rate is defined as the fraction of found tracks that are not successfully reconstructed.

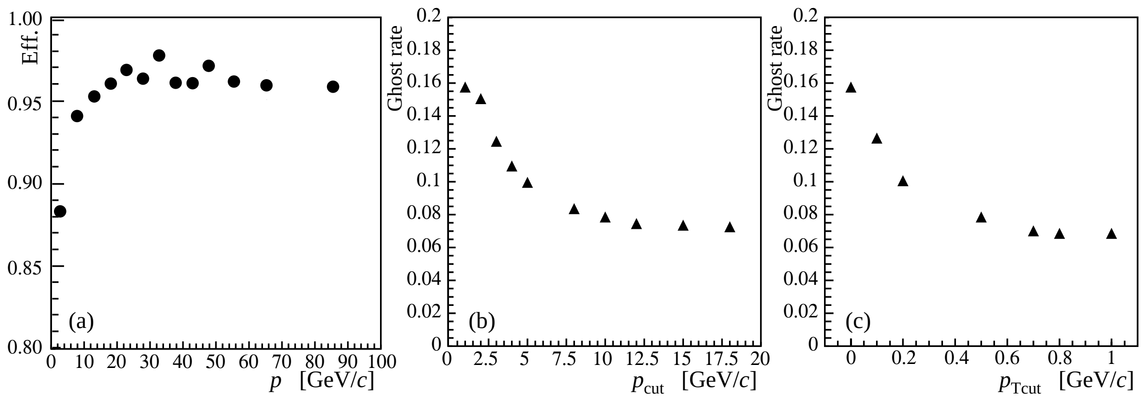

Figure 8: Performance of long track finding. (a) Efficiency as a function of the momentum of the generated particle. (b) The ghost rate, for tracks with reconstructed momentum greater than p_{cut}. (c) The ghost rate, for tracks with reconstructed transverse momentum greater than p_{Tcut}.

The average number of reconstructed tracks in $\mathrm{b\overline{b}}$ events is 74, which are distributed among the track types as follows: 27 long tracks, 10 V$\rightarrow$TT tracks, 10 T$\rightarrow$TT tracks, 23 VELO tracks and 4 T tracks. The track finding performance is summarized below for the most important cases: the long tracks, low momentum (V$\rightarrow$TT) tracks and $\mathrm{K^0_S}$ decay (T$\rightarrow$TT) tracks.

Long tracks: The average efficiency of long track reconstruction is 92%, with a corresponding total ghost rate of 16%. For long tracks the VELO track search algorithm has an efficiency of 96% with a ghost rate of 4%, and the T track search algorithm has an efficiency of 96% with a ghost rate of 12%. As shown in Fig. 8, an efficiency of over 95% is obtained for tracks with momentum greater than 5 GeV/c. The average efficiency to reconstruct the final state tracks in $\mathrm{B^0} \rightarrow \pi^+\pi^-$ and $\mathrm{B^0_s} \rightarrow \mathrm{D^-_s}\pi^+$ decays is 96%. Note that the reconstructed momentum and transverse momentum of ghost tracks peak at low values. Since the majority of B decay tracks have $p_{\mathrm{T}} > 0.5\,\mathrm{GeV}/c$ the effective ghost rate for physics reconstruction is approximately 8%.

Distributions of the total number of hits and the fraction of correctly assigned hits are shown in Fig. 9 for tracks which have been successfully reconstructed.

V$\rightarrow$TT tracks: The dependence of the efficiency and ghost rate on the momentum of V$\rightarrow$TT tracks is shown in Fig. 10. Also here the reconstructed ghost tracks are mainly of very low momentum. Since most tracks with $p < 1$ GeV/c are below threshold in RICH-1 the relevant efficiency for this procedure is ∼75% with a corresponding ghost rate of ∼12%.

T$\rightarrow$TT tracks: As described above, the T$\rightarrow$TT tracks are used to find $\mathrm{K^0_S}$ decays occurring outside the VELO region. The average efficiency for finding $\mathrm{K^0_S}$ decay pions with this procedure is 75%, with a dependence on momentum as shown in Fig. 11 (a). About 8 ghost tracks of this type are found per event, but they can be eliminated

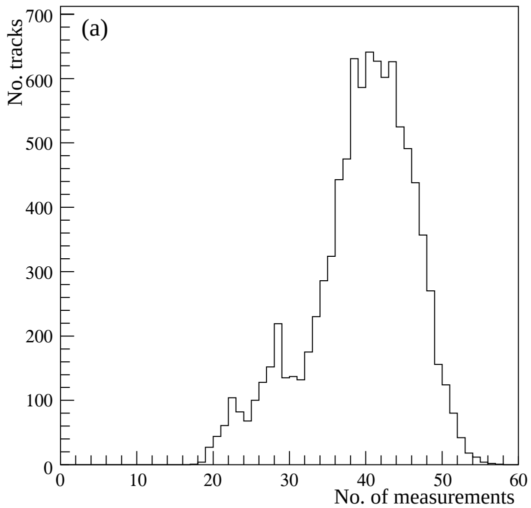

Figure 9: (a) The number of detector measurements assigned to a reconstructed long track, and (b) the fraction of hits which are correctly assigned.

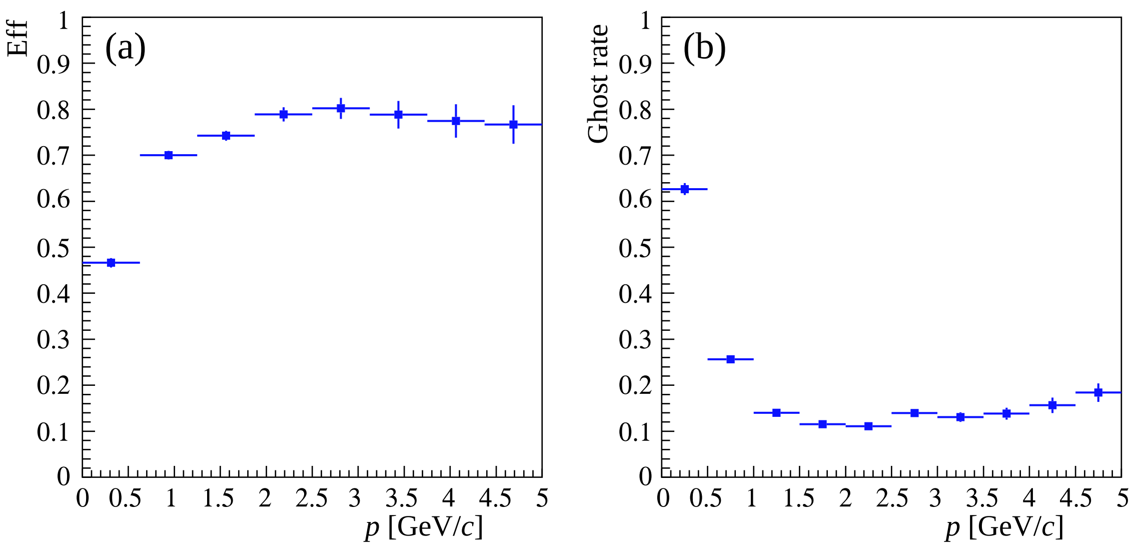

Figure 10: (a) V→TT tracking efficiency as function of momentum. (b) V→TT ghost rate as a function of momentum.

in the K^0_S search. Figure 11 (b) shows the invariant mass distributions for opposite sign T→TT tracks with a common vertex and with $p_T > 250\,\mathrm{MeV}/c$, in a sample of $B^0 \to J/\psi\, K^0_S$ events. The efficiency to find such "non-VELO" K^0_S decays is 54%. Figure 12 shows the invariant mass of the reconstructed B mesons using those K^0_S. It shows that the K^0_S combinatorial background seen in Fig. 11 (b) is not important once B mesons have been reconstructed. Detailed studies on the background from other decay modes are in progress.

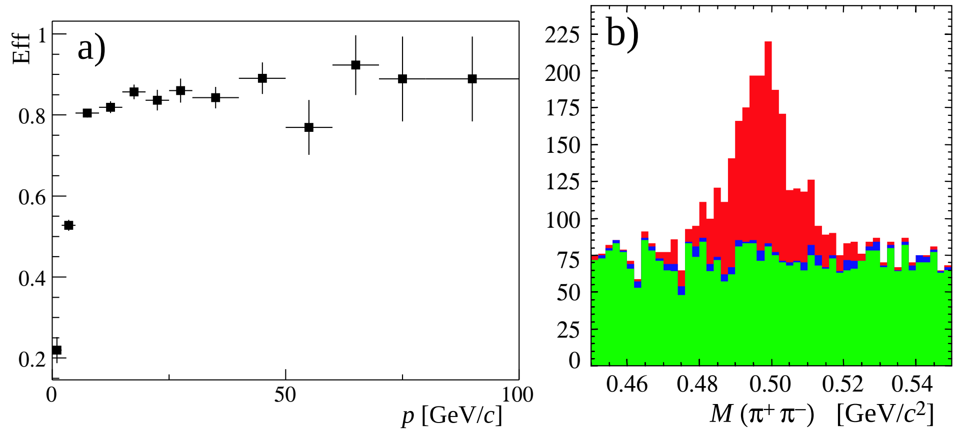

Figure 11: (a) T→TT tracking efficiency as function of momentum. (b) Invariant mass distribution of opposite sign T→TT tracks.

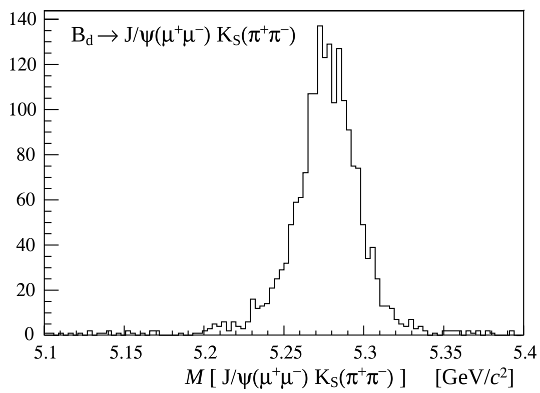

Figure 12: Invariant mass distribution of $\mathrm{J}/\psi(\mu^+\mu^-)\mathrm{K}^0_\mathrm{S}$ for signal events using K^0_S reconstructed from T→TT tracks.

4.2 Track fit

After tracks have been found their trajectories are refitted with a Kalman filter fit [31]. At a given z-position in the experiment a track is represented by the state vector $(x,\, y,\, S_x = dx/dz,\, S_y = dy/dz,\, q/p)$.

The initial state of the iterative Kalman procedure is obtained from the pattern recognition algorithms and taken at the most downstream measurement. The fit then proceeds in the upstream direction, updating the state vector at each measurement plane. As it traverses the detector the fit retrieves from the geometry database any (inactive) layers of material encountered. It allows for “kinks” in the trajectory due to multiple scattering and in addition corrects for dE/dx energy loss. As soon as the most upstream measurement has been reached the fit reverses direction in order to update the downstream track states with the full information of all measurements. In the standard reconstruction the track state and covariance matrix are specified at six z-positions in the experiment: the nearest point to the beam line, the most upstream measurement, and the entrance and exit points of the two RICH detectors.

The quality of the reconstructed tracks is monitored by the χ^2 of the fit and

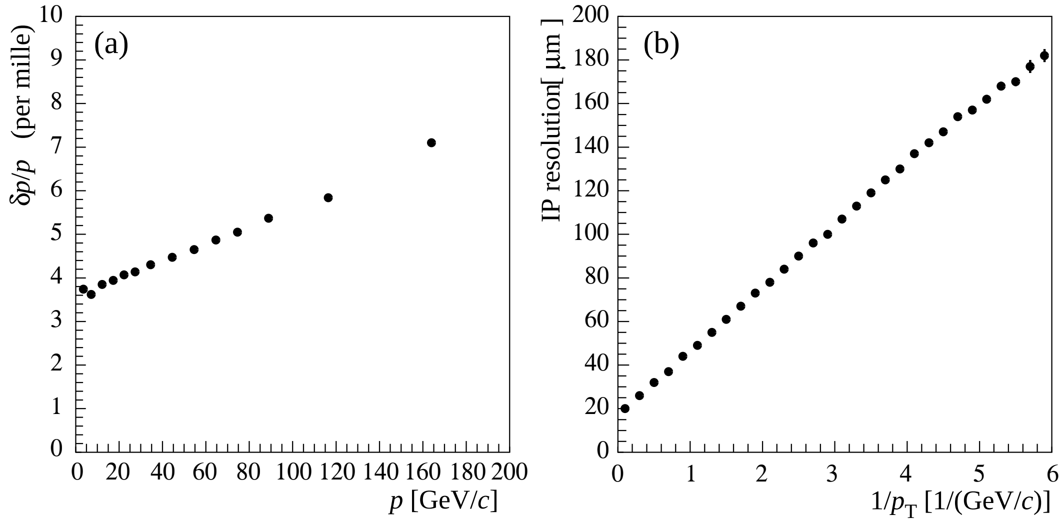

Figure 13: Resolution on the reconstructed track parameters at the production vertex of the track: (a) momentum resolution as a function of track momentum, (b) impact parameter resolution as a function of $1/p_{\mathrm{T}}$.

the "pull" distributions of the track parameters. The assigned errors of the fitting procedure for (x, y, S_x, S_y) are correct to within 5%, while the assigned momentum error is correct to within 20%. The latter is attributed to non-Gaussian multiple scattering effects along the trajectory.

The momentum resolution for long tracks is plotted as a function of the track momentum in Fig. 13 (a). The resolution is very similar to that of the Outer Tracker TDR set-up [2]: the reduction in material (and thus of multiple scattering distortions) approximately compensates the reduction of measurement planes.

The impact parameter resolution is plotted in Fig. 13 (b) as a function of $1/p_{\mathrm{T}}$ of the track. The resolution can be parametrized as $\sigma_{\mathrm{IP}} = 17\,\mu\mathrm{m} + 32\,\mu\mathrm{m}/p_{\mathrm{T}}$, for p_{T} in GeV$/c$. B decay products have a typical precision on their impact parameter in the range 20–40 μm.

The momentum resolution of V$\rightarrow$TT and T$\rightarrow$TT tracks are worse, as they do not traverse the full spectrometer. The T$\rightarrow$TT tracks see most of the magnetic field, leading to an average momentum resolution of $\delta p/p = 0.43\%$. The V$\rightarrow$TT tracks only see a small fraction of the total field integral and have a momentum resolution $\delta p/p \sim 20\%$.

4.3 Robustness tests

The track reconstruction efficiency depends only mildly on the total number of hits in the VELO, IT and OT detectors. This has been tested for long tracks in three ways:

1. In Fig. 14 the efficiency for tracks with $p > 5$ GeV$/c$ and the ghost rate are plotted as a function of a "relative" multiplicity parameter, defined as:

$$N_{\mathrm{rel}} = \frac{1}{3}\left[\frac{N_{\mathrm{VELO}}}{\langle N_{\mathrm{VELO}}\rangle} + \frac{N_{\mathrm{IT}}}{\langle N_{\mathrm{IT}}\rangle} + \frac{N_{\mathrm{OT}}}{\langle N_{\mathrm{OT}}\rangle}\right]$$

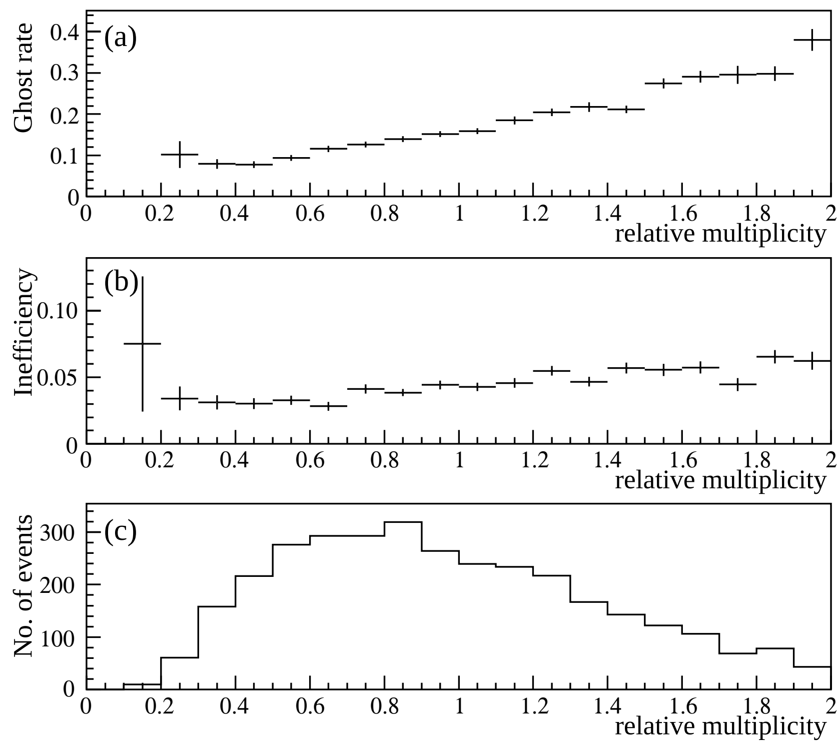

Figure 14: (a) The ghost rate plotted versus the relative multiplicity, (b) the inefficiency ($1-\varepsilon$) plotted versus the relative multiplicity, and (c) the relative multiplicity distribution, for long tracks.

The relative multiplicity is seen to fluctuate significantly on an event-to-event basis, however the changes in efficiency are small, for corresponding ghost rates which rise linearly from 6% (for quiet events) up to 30% (for very hot events, with a factor of two more hits).

2. The efficiency and ghost rate have been compared for different settings of the PYTHIA tuning parameter $p_{\mathrm{T}}^{\mathrm{min}}$ (see Section 2) between 3.47 (default) and 2.96 (-3σ deviation) GeV/c. For the latter value the average number of tracks increases by 20%. No substantial effect is observed on the reconstruction efficiency, while the ghost rate increases by 1%. The tracking performance is thus not very sensitive to the exact tuning of PYTHIA.

3. In Fig. 15 the efficiency and ghost rate are plotted as a function of the number of visible interactions in the event. The efficiency is not strongly dependent on the number of interactions, while the ghost rate increases by approximately 6% for each additional interaction. It should be noted that at nominal luminosity events with single or double interactions dominate (see Table 1 in Section 2), while the Pile-up Veto will further suppress events with multiple interactions (see Section 6.1).

The track reconstruction efficiency does not depend critically on the Inner and Outer Tracker single-channel efficiency. Figure 16 shows the track reconstruction

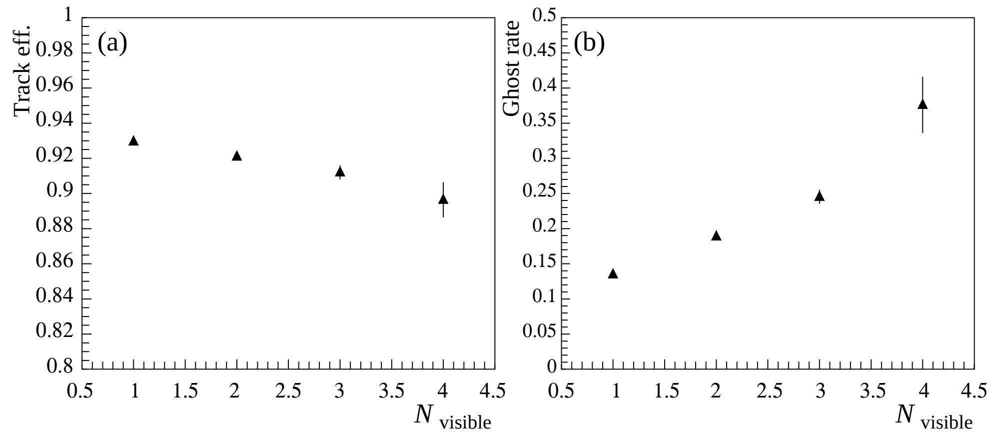

Figure 15: (a) The long track efficiency, and (b) the ghost rate, plotted as function of the number of visible interactions.

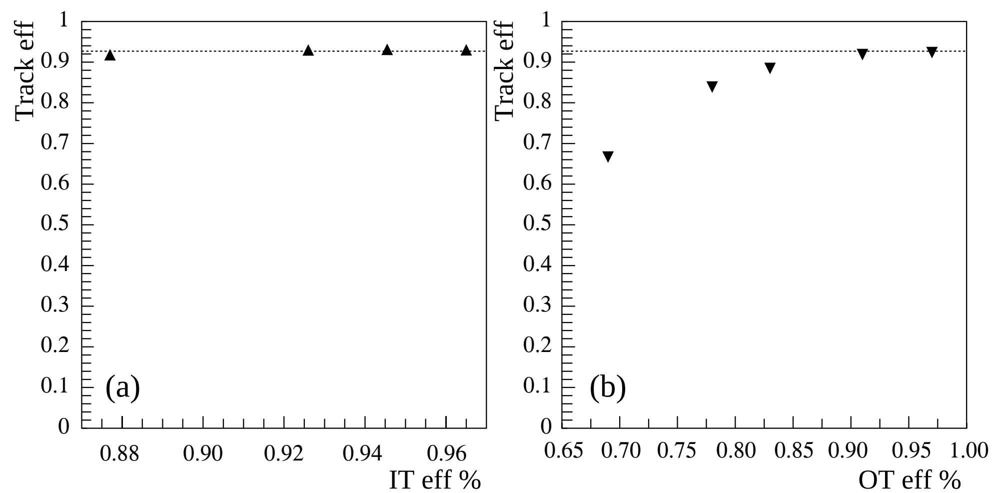

Figure 16: (a) The reconstruction efficiency of tracks passing through the IT as function of the hit efficiency of the IT. (b) The reconstruction efficiency of tracks passing through the OT as function of the hit efficiency of the OT.

efficiency when the hit efficiencies of the IT and OT are reduced. In both cases the tracking performance is stable if additional inefficiencies up to $\sim$10% are introduced. For the Outer Tracker an inefficient layer in one detector module would correspond to a hit inefficiency of 0.23%, and have no significant effect on the track reconstruction efficiency. The unlikely case of a fully inefficient detector plane would imply a 4% hit-efficiency reduction and have an effect of $\sim$1% on the track reconstruction efficiency. The tracking efficiency for the VELO is observed to reduce by 1.1%, 2.5% or 5.5% if the fraction of randomly generated dead strips in each detector is set to 0.5%, 1% or 2% respectively. This greater sensitivity compared to the IT/OT is ascribed to the tuning of the current off-line algorithm, since an alternative algorithm used in the Level-1 trigger is less sensitive to dead strips.

Adding as many additional noise hits as the number of real hits, a negligible effect is seen on the tracking performance.

5 Particle Identification

Particle identification within LHCb is provided by the two RICH detectors, for hadrons, along with the Calorimeter system for electrons and the Muon detector for muons. Technical details concerning these systems can be found in their respective TDRs [5, 32, 7].

5.1 RICH particle identification

Particle identification with the RICH system is performed as follows. The pattern of hit pixels observed in the RICH photodetectors is compared to the pattern that would be expected under a given set of mass hypotheses for the reconstructed tracks passing through the detectors, using the knowledge of the RICH optics. A likelihood is determined from this comparison, and then the track mass-hypotheses are varied so as to maximise the likelihood. In the high track multiplicity environment typical of LHCb events, the main source of background photons in the RICH detectors is from neighbouring tracks. By maximising the global likelihood for all found tracks, this background is optimally controlled. Details of the method can be found elsewhere [33].

As mentioned in Section 4.1, at the time of the Technical Proposal [1] there was no pattern recognition for the tracking, just a set of quality criteria that were applied to the tracks. Pattern recognition for the RICH system was available, but used only for a detailed study in the $B^0 \to \pi^+\pi^-$ channel; for the other physics channels a fast parametrization of the RICH performance was used. By the time of the RICH TDR, more extensive studies had been made of the RICH pattern recognition performance [34], but the tracking pattern recognition was still ideal. Since the TDR, full pattern recognition is now in place for all steps of the event reconstruction. Thus the quality of the reconstructed tracks includes the effects of imperfect assignment of hits to tracks and of ghost tracks.

Since the RICH TDR the description of the detector has changed somewhat: the material budget has been reduced where possible, in particular for the mirrors and their supports in RICH-1, and by changing the material of the beam pipe from aluminium to beryllium for the first section and Be/Al alloy for the second section. The consequence of this effort can be seen in Fig. 17, where the current hit-pixel multiplicity in the two RICH detectors is compared to that of the TDR (for $b\bar{b}$ events in single-interaction bunch crossings). There has been a significant reduction in the number of hit pixels per event, largely due to the reduction of background particles from secondary interactions. The effect is less pronounced in RICH-2, as it is compensated somewhat by the 20% increase in radiator length that was introduced between the TDR and EDR [35].

Another major change for the RICH system since the TDR has been the redesign of RICH-1, to adapt to the magnetic field that has been introduced between the VELO and TT station for the Level-1 trigger, as described in the Introduction. As a consequence, local shielding has to be provided for the RICH photon detectors, and this has been achieved by adjusting the optics, introducing a second (flat) mirror in a

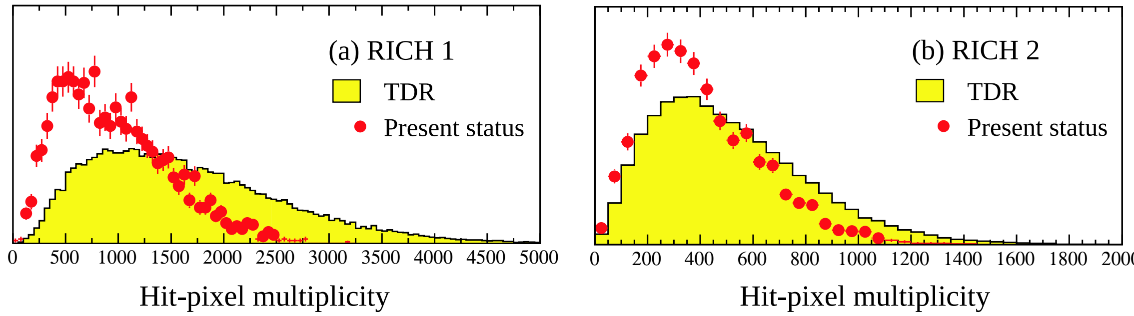

Figure 17: Hit-pixel multiplicity in the RICH detectors (a) RICH-1, (b) RICH-2.

similar fashion to RICH-2. This new optical layout is now included in the simulation, and leads to a slight reduction in the number of detected photoelectrons per track (for high momentum tracks) from the gas radiator of RICH-1, as shown in Table 2. This is due to the ~90% reflectivity of the extra mirror. A similar effect is not seen in the number of detected photoelectrons from aerogel, as the reoptimized optical layout has allowed a larger fraction of the aerogel image to be covered for the same overall size of photon detector plane. For RICH-2 the expected increase from the extended radiator length is observed. The angular resolution per photoelectron has not changed significantly since the TDR.

The effect of the curvature of the tracks in the low magnetic field that has been introduced into the RICH-1 region has been studied and is small: for the photons from the gas radiator of RICH-1, it gives rise to an angular smearing given approximately by $4\,\mathrm{mrad}/p$ for p in GeV/c. This is negligible for tracks above a few GeV/c, and for the lowest momentum tracks the separation is dominated by the aerogel radiator, which is unaffected.

To study the performance of the RICH system, "long" tracks (passing through the full spectrometer, as defined in Section 4.1) have been studied in a sample of $\mathrm{B_s^0} \to \mathrm{K}^-\pi^+$ events. For those which are matched to true pions, the difference in likelihood between assuming the pion and kaon hypothesis in the RICH analysis is determined. This can be converted into the significance of π–K separation, $\Delta\sigma = \sqrt{2\,|\Delta \ln \mathcal{L}|}$, signed according to the difference in log-likelihood, $\Delta \ln \mathcal{L}$. The distribution of this significance can be seen as a function of momentum in Fig. 18 (a). The few negative entries correspond to tracks for which the kaon hypothesis was preferred over the pion hypothesis. The average of this distribution is shown in Fig. 18 (b), and illustrates that substantial π–K separation is achieved over almost all of the momentum range

Table 2: Average number of detected photoelectrons per saturated track in the three RICH radiators, compared to the numbers in the TDR.

Radiator	N_{pe} (now)	N_{pe} (TDR)
Aerogel	6.8	6.6
C_4F_{10} gas	30.3	32.7
CF_4 gas	23.2	18.4

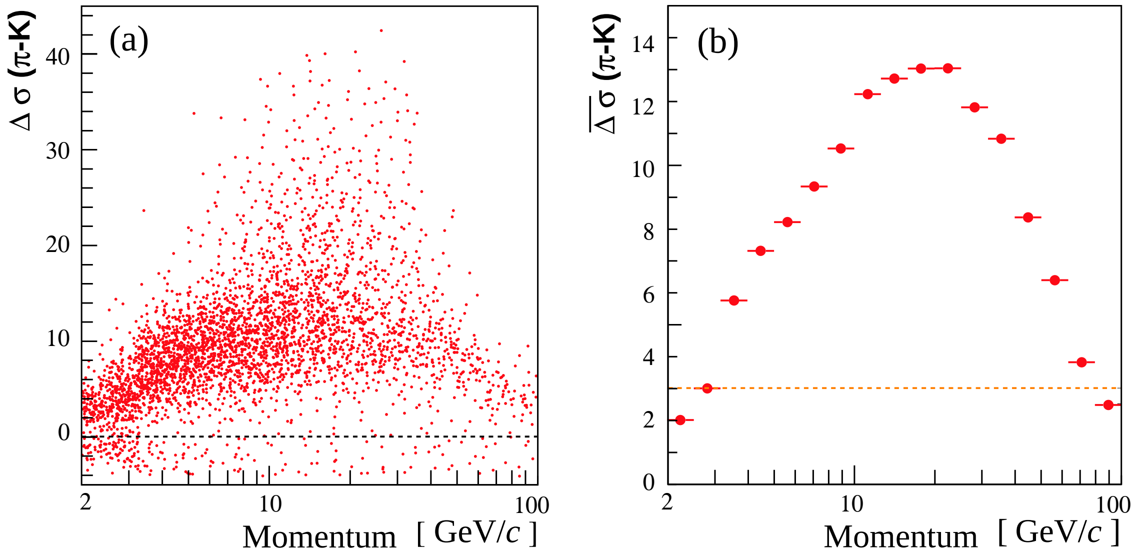

Figure 18: K–π separation in sigma as a function of momentum for true pions (a) for each track in the sample (b) the average.

of interest, $2 < p < 100\,\mathrm{GeV}/c$.

Care should be taken when interpreting these π–K separation figures in terms of "sigma", as the behaviour is not Gaussian, as is evident from Fig. 18 (a). More relevant is the performance expressed as the efficiency for reconstructing kaons, viewed in conjunction with the misidentification rate for pions. These are shown as a function of momentum in Fig. 19, and compared to the values quoted in the TDR. Again the plots are made for "long" tracks, in single-interaction events; the effect of including multiple-interaction effects is only at the percent level here. Tracks are identified as kaons if their maximum-likelihood hypothesis is kaon or heavier, and as pions if it is pion or lighter. In the kaon efficiency plot, Fig. 19 (a), the effect of crossing the thresholds for Cherenkov light production in the three radiators is evident at $p \sim 2$, 9 and $16\,\mathrm{GeV}/c$. The performance is comparable to that quoted in the TDR, despite the fact that the track reconstruction is now made with full pattern recognition. The average efficiency for kaon identification between 2 and $100\,\mathrm{GeV}/c$ is 88%. The pion misidentification rate, $\epsilon(\pi \to \mathrm{K})$, shown in Fig. 19 (b), is also similar to that of the TDR, except for a higher misidentification rate in the momentum region 30–$70\,\mathrm{GeV}/c$. This corresponds to a region of higher kaon efficiency, and further tuning of the background parametrization used in the likelihood calculation can play off one against the other, according to the needs of the physics analyses. The average pion misidentification rate between 2 and $100\,\mathrm{GeV}/c$ is 2.7%.

This performance was achieved with the use of all classes of tracks discussed in Section 4.1.1, including in particular the V$\to$TT tracks: these help in the description of the observed photon distributions in RICH-1. The use of the V $\to$ TT tracks for the RICH reconstruction was not ready in time for the physics studies presented in Section 7, so they were performed with a poorer kaon identification efficiency at low momentum. The improved performance shown here will be applied for the final results to be presented in the Reoptimization TDR.

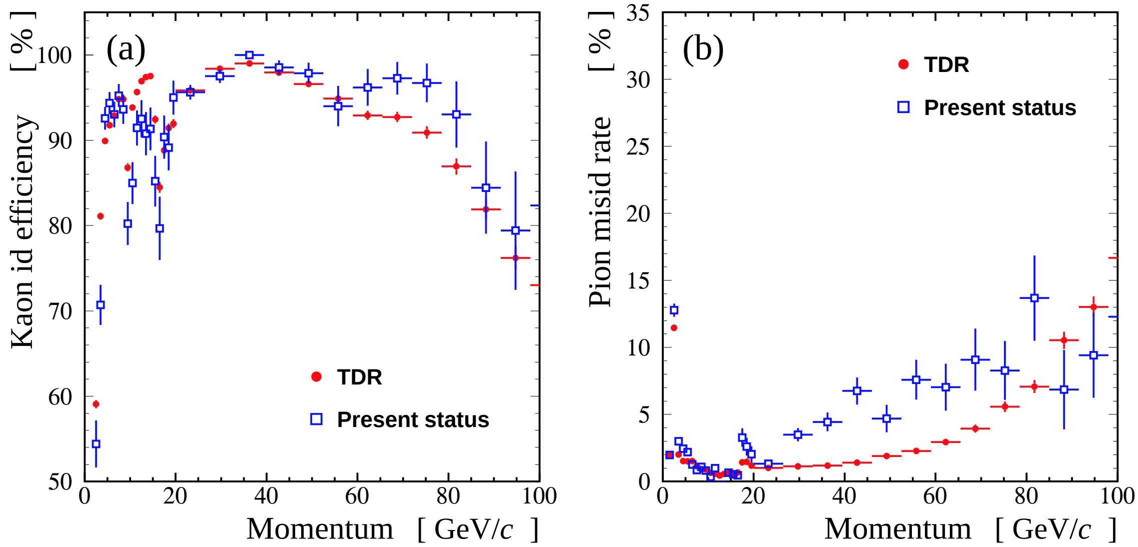

Figure 19: (a) Kaon identification efficiency, (b) pion misidentification rate as a function of momentum.

5.2 Lepton identification

Muon identification is performed through the comparison of the hits in the Muon detector with the extrapolation of a reconstructed track. For details see [7]. A small gain in performance can be achieved by combining the RICH information with that from the Muon detector, but this has not yet been exploited. The average muon identification efficiency is currently 86% for muons from $\mathrm{J}/\psi \rightarrow \mu^+\mu^-$ decays in $\mathrm{B}^0 \rightarrow \mathrm{J}/\psi\,\mathrm{K}^0_\mathrm{S}$ events, using selection cuts which have been tuned to give a pion misidentification rate $\epsilon(\pi \rightarrow \mu) = 1.0\%$. The high purity that can be achieved with such cuts is illustrated in Fig. 20 (a), where the $\mu^+\mu^-$ mass plot is shown at the first step in the analysis of $\mathrm{B}^0_\mathrm{s} \rightarrow \mathrm{J}/\psi\,\phi$ events, taking all oppositely charged pairs of tracks from signal events that pass the muon identification requirements. As can be seen, a clean J/ψ mass peak is reconstructed with a resolution of about $13\,\mathrm{MeV}/c^2$.

For electron identification the Calorimeter system is used. The ECAL is used to compare the cluster energy with the momentum of the associated track. A search is also made for bremsstrahlung photons emitted by the electron candidates in material before the magnet: as there is little material within the magnet, such neutral clusters are expected in a well defined position given by the electron track extrapolation from before the magnet. If found, their energy is added to that of the track, and the confidence level that the track is an electron is increased. In addition the deposit of energy in the Preshower is also used to improve the electron identification. Finally, the information from the calorimeter is combined with the information from the RICH, by combining the likelihoods, which gives a significant improvement in the electron identification performance. Still under study is the additional information that could be used from the HCAL.

The J/ψ mass plot for the electron mode is shown as the open points in Fig. 20 (b). The signal is fit with a function including a radiative tail, to account for the imperfect

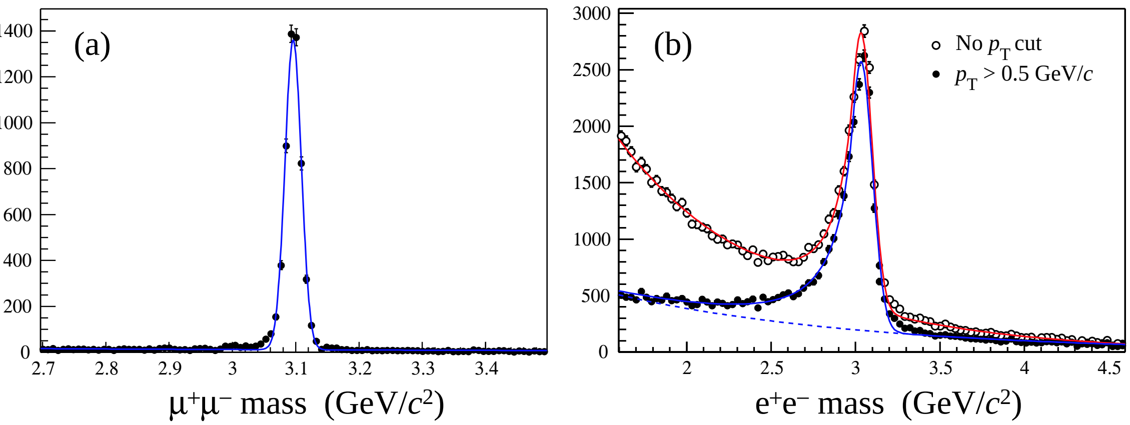

Figure 20: Mass plots for the reconstruction of $J/\psi \to \ell^+\ell^-$ decays in $B_s^0 \to J/\psi\,\phi$ signal events: (a) for $\ell = \mu$ (b) for $\ell = e$, where the open points are before any p_T cut, and the solid points are after requiring $p_T > 0.5\,\mathrm{GeV}/c$ for the $e^\pm$ candidates.

correction of bremsstrahlung. The background is larger than in the muon channel, and is either due to real (secondary) electrons, or due to one of the pair of tracks being a ghost track; the contribution from misidentified hadrons is very small. These background tracks are dominantly of low p_T, and can be efficiently rejected by applying the requirement $p_T > 0.5\,\mathrm{GeV}/c$ for the electron candidates, as shown by the solid points in Fig. 20 (b). The average efficiency for reconstructing electrons from $J/\psi \to e^+e^-$ decays in $B^0 \to J/\psi\,K_S^0$ events is 78%, for cuts which have been tuned to give a pion misidentification rate $\epsilon(\pi \to e) = 1.0\%$.

6 Trigger

The LHCb Trigger contains three levels, called Level-0 (L0), Level-1 (L1) and Higher Level Trigger (HLT).

L0 uses information from the Pile-up Veto, the calorimeters and the muon chambers. All electronics is implemented in full custom boards, however only commercial components are used. Part of the functionality of the calorimeter triggers is placed in an environment which is expected to receive a few hundred rad per year, all other hardware is housed in the radiation-free electronics barracks. All triggers use a fully synchronous implementation, i.e. their latency does not depend upon occupancy nor on history. The front-end electronics allow a maximum latency of 4 μs, and the maximum output rate is limited to 1.1 MHz due to the multiplexing of the FE electronics of the other sub-systems.

L1 is based on the VELO, TT and the summary information of L0. The trigger algorithm is implemented on a commodity CPU farm. Its maximum output rate is 40 kHz, at which rate full event building is performed.

HLT has access to the full event data, and is executed on a commodity CPU farm. The algorithm first confirms the L0 and L1 triggers with better precision, and then will mimic the off-line selection algorithms for the various channels to reduce the rate to 200 Hz, at which rate events will be written to storage. The HLT algorithms are under development, and will be described in more detail in the forthcoming Trigger TDR.

As in the Technical Proposal [1] L0 and L1 are fully simulated in the standard LHCb software framework and will be described below in more detail.

6.1 Level-0 trigger

The L0 trigger has two distinct components: on the one hand B-meson decay products such as large E_T leptons and hadrons are reconstructed, while on the other hand global event variables such as the number of interactions and multiplicities are collected. The former are used to distinguish interactions with interesting B-meson decays from the minimum-bias background, while the latter are used to assure that the events are selected based on the B signature rather than due to large combinatorics, and that these events will not occupy a disproportional fraction of the data-flow bandwidth or available processing power.

The muon chambers allow stand-alone muon reconstruction with a p_T resolution of $\sim 20\%$ [7]. The chambers are subdivided into 120k pads and strips, and the requirement is that each chamber has a $>99\%$ efficiency, which is obtained by OR-ing two layers per station. Despite the reduction in the number of planes in M1 from four to two, it has been found that the efficiency of the muon trigger remains unchanged even if the hit efficiency of each of the two layers were to drop to as low as 80%. Pads and strips are combined to form 26k so-called logical pads, which range in size from $1.0\times2.5\,\text{cm}^2$ near the beam to $25\times31\,\text{cm}^2$ for the pads in M5 furthest away from the beam. All pads are projective in the non-bending plane. One crate per quarter houses the trigger boards which reconstruct the two muons with the largest p_{T} [36]. There are no cross connections between the crates, and hence muons crossing the quarter boundaries are not reconstructed.

The calorimeter system [32] provides the following information for the L0 trigger:

1. The Electromagnetic Calorimeter (ECAL) is of the shaslik type, 25 radiation lengths thick, contains 5952 cells, and provides 8-bit E_{T} information per cell.

2. The Preshower (PS) collects the light after 2.5 radiation lengths of lead, is also subdivided in 5952 cells, and provides one bit per cell for e/π separation by setting a threshold that depends on the radial position of the cell.

3. The Scintillating Pad Detector (SPD) distinguishes between charged and neutral particles which produce a shower in the ECAL, and consists of 5952 cells, providing one bit per cell.

4. The Hadronic Calorimeter (HCAL) is constructed of iron/scintillating tiles subdivided into 1468 cells and also provides 8-bit E_{T} information per cell.

The implementation of the calorimeter trigger [37] is based on forming clusters by adding the E_{T} of 2×2 cells, and selecting the clusters with the largest E_{T}. Clusters found in the ECAL are identified as e,γ or hadron depending on the information from the PS and SPD. The largest HCAL clusters have the energy of the corresponding ECAL cluster added to them if this ECAL cluster is the largest cluster in an area of 4×8 cells and matches the HCAL cluster position. By summing all transverse energy in 4×8 cells in the ECAL so-called local-π^0 candidates are formed. Largest E_{T} clusters on neighbouring groups of 4×8 cells in the ECAL are combined to form so-called global-π^0 candidates. The E_{T} of all HCAL cells is summed to provide global event information to allow an interaction trigger. The total number of SPD cells with a hit are counted to provide a measure of the charged track multiplicity in the crossing. Figure 21 shows the off-line execution times for finding long tracks as a function of the SPD multiplicity. Rejecting all events above a multiplicity of 380 at L0 reduces the tail in the execution times drastically, while, due to the possibility of lowering the L0 thresholds for the remaining events, it also results in a small increase in the overall useful event yield.

The Pile-up Veto aims at distinguishing between crossings with single and multiple visible interactions. It uses four silicon sensors of the same type as those used in the VELO to measure the radial position of tracks. The sensors are subdivided in two stations located upstream of the interaction point, covering $-4.2 < \eta < -2.9$. For tracks coming from the beam-line the radial position r of a track passing the two stations at z_A and z_B is related to their origin by

$$z_{\mathrm{vertex}} = \frac{r_B z_A - r_A z_B}{r_B - r_A}.$$

The sensors provide 2048 binary channels using the Beetle front-end chip [38]. The radial hits are projected into an appropriately binned histogram according to the

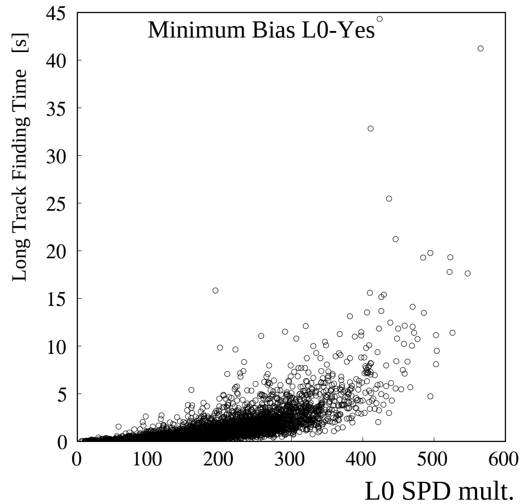

Figure 21: The reconstruction time of events as a function of the SPD multiplicity, which is 170 hits on average for events which are accepted by L0.

above relation using FPGAs [39]. All hits contributing to the highest peak in this histogram are masked, after which the height of the second peak is a measure of the number of tracks coming from a second interaction in the crossing. Figure 22 illustrates the performance of the Pile-up Veto. Apart from the backward track multiplicity in the first and second vertex found, the Pile-up Veto furthermore provides the position of these vertex candidates along the beam-line and the total hit multiplicity in the two stations. The Pile-up Veto information allows a relative luminosity measurement.

The L0 Decision Unit (L0DU) collects all information from L0 components to form the L0 Trigger, i.e. the largest $E_{\rm T}$ e, γ, $\pi^0_{\rm local}$, $\pi^0_{\rm global}$, and the two largest $E_{\rm T}$ hadron clusters. Global event variables are also collected: the SPD multiplicity, and the sum of the transverse energy of the HCAL of the actual crossing, and of the two preceding and following crossings. From the possible eight muons provided by the four quadrants of the muon trigger the three largest in $p_{\rm T}$ are selected. Finally the Pile-up Veto information is also used. The L0DU is able to perform simple arithmetic to combine all signatures into one decision per crossing. The algorithm employed at the moment accepts events where at least one of the largest $E_{\rm T}$ e, γ, $\pi^0_{\rm local}$, $\pi^0_{\rm global}$, hadrons or muons is above the trigger threshold for the respective particle type, providing the Pile-up Veto detects less than three tracks coming from a second primary vertex. Events are also accepted if the sum of the $p_{\rm T}$ of the two muons with the largest transverse momentum are above a threshold, irrespective of the Pile-up Veto result. Other global event variables like hit multiplicities of the Pile-up Veto and SPD are not yet used in the results presented below, but instead are considered as contingency.

The above mentioned thresholds have to be set such that the 1.1 MHz maximum output rate of L0 is not exceeded. The following procedure is used to weigh the

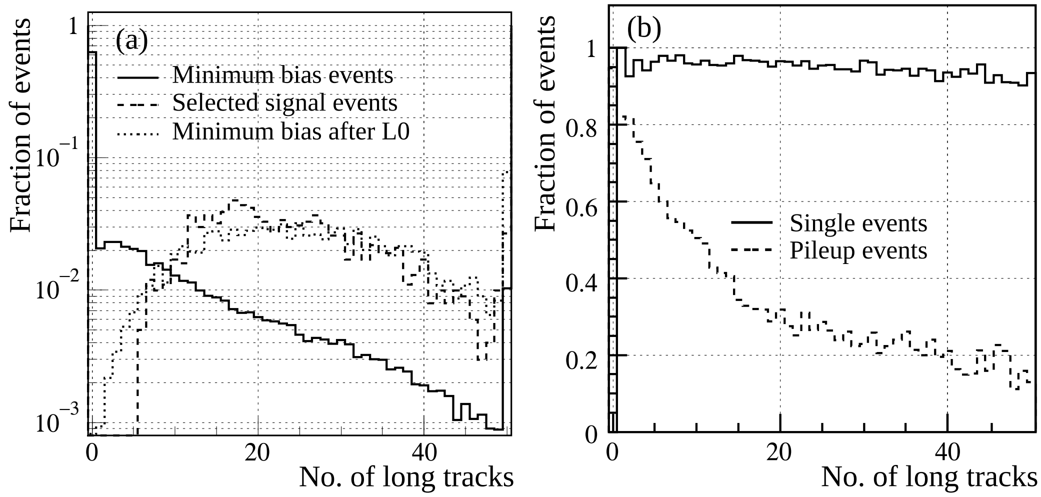

Figure 22: (a) Fraction of events as a function of the number of long tracks in the spectrometer for minimum-bias events (full line), off-line selected signal events (dashed line) and minimum-bias events which are accepted by L0 (dotted line). The last bin contains all events with 50 tracks or more. (b) The full line shows the fraction of events accepted by the Pile-up Veto for a single interaction per crossing as a function of the number of long tracks. The dashed line shows the same fraction in events with multiple interactions as a function of the number of long tracks not originating from the same vertex as the B mesons in the event.

various trigger components:

1. The L0 output rate is fixed to 90% of the available output rate, hence 1 MHz, to leave 100 kHz as contingency. Beam related background, notably from halo muons, has been studied, but with our current understanding should produce a negligible rate. Even with gas densities ten times nominal, conditions which may occur at the start of running, the loss in efficiency is only a few percent.

2. For every given off-line selected channel, a scan is performed over the thresholds and Pile-up Veto requirements to give the best performance for that channel alone.

3. All channels are then combined, by looking for a setting where the loss of all channels relative to the best achievable is minimized.

Figure 23 shows the above mentioned relative loss for some channels as a function of the threshold on the highest p_{T} muon. Over a wide range of the muon p_{T} threshold the losses for all considered channels are kept well below 10%. Table 3 shows the efficiency of the L0 trigger for events which pass the off-line selection criteria.

The results shown depend on the track multiplicity and p_{T} distributions of the generated events. This sensitivity will be determined by comparing different generators at various settings in the Trigger TDR. Ignoring the small rate of large E_{T} clusters due to overlapping clusters in the calorimeters, the sensitivity of L0 to the

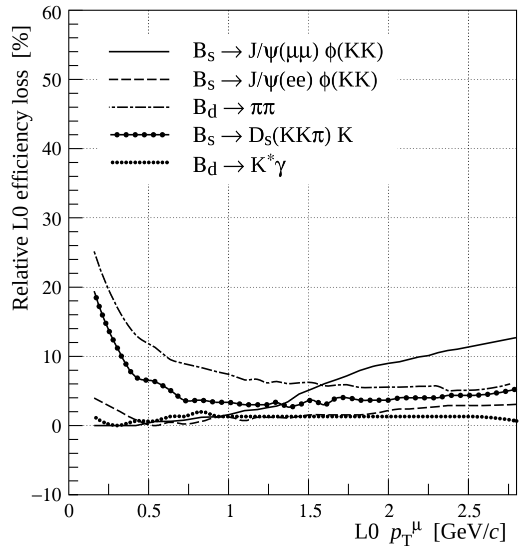

Figure 23: The relative loss of L0 trigger efficiency as defined in the text as a function of the highest p_{T} muon threshold for a total L0 output rate of 1 MHz. For a large range of thresholds the losses are small, and the overall loss is minimized for $p_{\mathrm{T}}^{\mu} = 1.23\,\mathrm{GeV}/c$.

Table 3: Efficiencies of the L0 trigger relative to off-line selected events.

Channel	$\pi^+\pi^-$	$\mathrm{D_s^{\mp}K^{\pm}}$	$\mathrm{J}/\psi(\mu^+\mu^-)\phi$	$\mathrm{J}/\psi(\mathrm{e^+e^-})\phi$	$\mathrm{K}^{*0}\gamma$
L0-eff (%)	61	44	93	52	82

track multiplicity in the event is proportional to the increase in L0 output rate for fixed thresholds. Figure 24 shows the efficiency of L0 for a few selected channels as a function of the L0 output rate. An output rate of $\sim$500 kHz for events produced with the present PYTHIA settings corresponds to an output rate of $\sim$1 MHz in case the track multiplicity would be twice as large, since the L0 retention is small. Hence doubling the multiplicity would lead to a loss of 10–30% of the efficiency, depending on the channel. For a 50% increase in multiplicity the loss is less than 15% for all channels.

6.2 Level-1 trigger

The L1 trigger exploits the finite lifetime of the B mesons in addition to the large B-meson mass as a further signature to improve the purity of the selected events. The following information is used by L1:

1. The L0DU summary information as described in the previous section.

2. The VELO measurements of the radial and angular position of the tracks, in silicon planes perpendicular to the beam-line between radii of 8 mm and 42 mm.

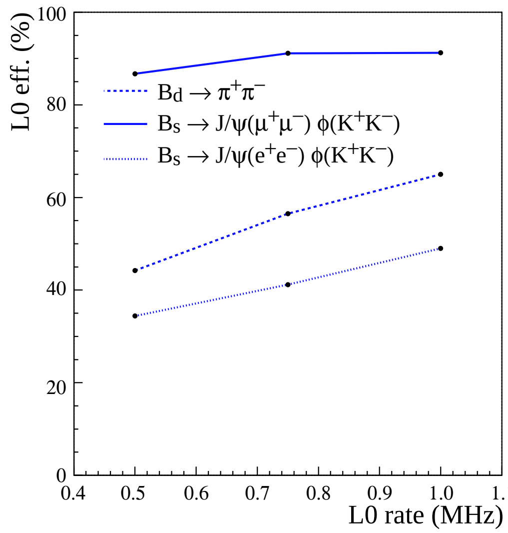

Figure 24: The efficiency of the L0 trigger for off-line selected signal events with only one interaction per crossing as a function of the L0 output rate.

The angular position is measured with quasi-radial strips with a stereo angle between 10–20°. A cluster search algorithm is performed in the 170k channels using FPGAs to find the roughly 1000 clusters per event.

3. The Trigger Tracker (TT) measurements from its four silicon planes, two with vertical strips and two with a $\pm 5°$ stereo angle. About 400 clusters are found in 144k channels using the same implementation as the VELO and a similar algorithm.

The L1 trigger algorithm will be executed on $\sim$500 commodity CPUs, and requires event building at 4 kbytes/event to be performed at a L0 output rate of 1.1 MHz.

B mesons with their decay products in the LHCb acceptance move predominantly forward along the beam-line, which implies that the projection of the impact parameter in the plane defined by the beam-line and the track is large, while in the plane perpendicular to the beam it is almost indistinguishable from primary tracks. The L1 algorithm exploits this by reconstructing so-called 2D tracks using only the VELO sensors which measure the radial position. The 2D track finding efficiency for charged tracks originating from a B-meson decay and inside the acceptance of the spectrometer is $\sim$98%. The 2D tracks are also sufficient to measure the position of the primary vertex since the strips at constant radius are segmented in 45° ϕ-slices. The RMS of the primary vertex resolution obtained is 170 μm and 50 μm in the directions along and transverse to the beam respectively. Figure 25 shows an event display of the result of the 2D track search in a 45° slice of the VELO. In this event 72 forward tracks are found in total, while the mean number of forward tracks in L1 events is 58.

Hence half of the clusters in the VELO are used to measure the impact parameter of tracks, and make a preselection on B-decay candidates. Using the sensors measuring the angular position, the candidate tracks with an impact parameter be-

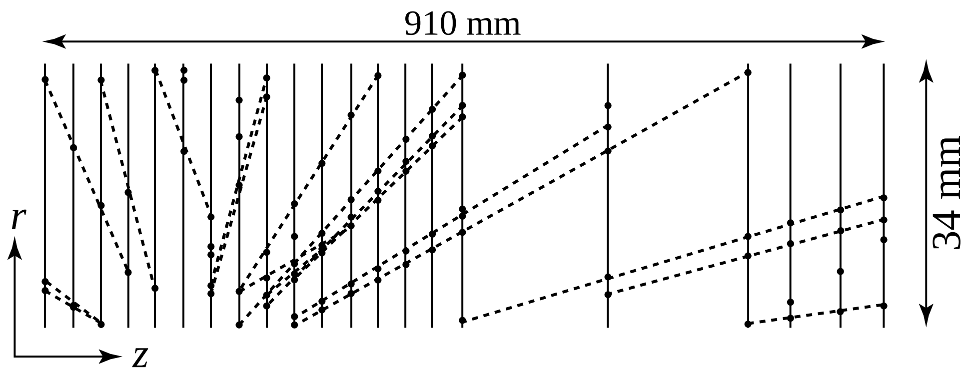

Figure 25: Event display of the result of the 2D tracking in the VELO detector, showing all hits and reconstructed tracks in a slice of 45° of the VELO R-sensors in an event where 72 forward 2D tracks were reconstructed.

tween 200 μm and 3 mm are then converted to tracks in three dimensions (3D tracks). The B-decay candidates are also matched to the electron and hadron clusters from the L0-calorimeter trigger, and the L0-muon candidates. In Fig. 26 the invariant mass formed from all oppositely-charged pairs of L0-muon candidates that have been matched to 3D VELO tracks is shown. A clear J/ψ signal can be seen, while in minimum bias events only a few kHz of the events have a $\mu\mu$-candidate with an invariant mass above 2 GeV.

About eight 3D tracks per event are selected based on their impact parameter and matched to hits in TT to measure their momenta. The 3D VELO tracks are considered matched if at least three hits are found in the four TT planes. The vertical component of the magnetic field between the VELO and TT is shown in Fig. 27, and compared to the field used for the TP. The present field allows a momentum resolution of about 20–40% depending on the momentum, which is sufficient to use the p_{T} of tracks as a B signature [10], and also allows the error on the impact parameter to be calculated including multiple scattering. The field in between the VELO and TT is parametrized to take its non-uniformity into account.

The final L1 trigger decision is made by combining the information for tracks with significant impact parameter, large p_{T} and possibly being matched to leptons and hadrons from L0. Figure 28 shows how the p_{T} and impact parameter significance are used to distinguish between the minimum-bias background events and, in this example, the channel $\mathrm{B}_{\mathrm{s}}^{0} \rightarrow \mathrm{D}_{\mathrm{s}}^{\mp}\mathrm{K}^{\pm}$. Events are selected according to the logarithmic sum of the p_{T} of the two VELO–TT tracks with the largest p_{T} in the event, and the logarithmic sum of their impact parameter significance, as shown in Fig. 28. Events are also accepted if the invariant mass formed from two oppositely-charged pairs of L0-muon candidates exceeds $2\,\mathrm{GeV}/c^2$. Channels with leptons in the final state especially profit from the matching between VELO tracks and L0-lepton candidates, while the VELO–TT and VELO–L0-hadron matching boosts the efficiency for hadronic final states compared to just exploiting the impact parameter information from the VELO. Figure 29 (a) shows the L1 efficiency for some off-line selected channels versus the L1 output rate.

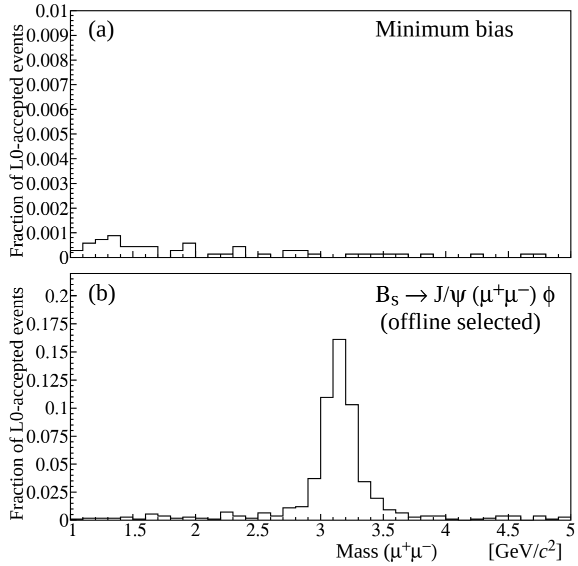

Figure 26: Invariant mass of J/ψ candidates, for which the muons have been reconstructed by combining VELO tracks with the L0 muon information.

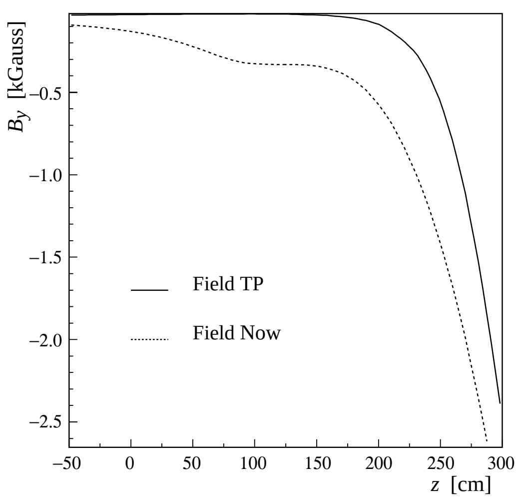

Figure 27: The vertical component of the magnetic field as used for the TP (full line), and the present field without the magnetic shielding plate but with the RICH-1 shielding boxes (dashed line).

To test the sensitivity to the event-generation model the minimum-bias events which are accepted by L0 were subdivided into three sub-samples based on the number of 2D tracks reconstructed in the VELO. The average 2D track multiplicity is 27 and 94 for the samples with less than 40 and more than 70 reconstructed 2D tracks respectively, while the sample with 40–70 tracks has a mean multiplicity of 55, which is similar to that of the whole sample. Figure 29 (b) shows the L1 performance for these three sub-samples for $B_s^0 \to D_s^{\mp}K^{\pm}$ events. From these results it can be inferred that if the mean multiplicity would increase by 70%, the L1 efficiency for this channel would decrease by 20%.

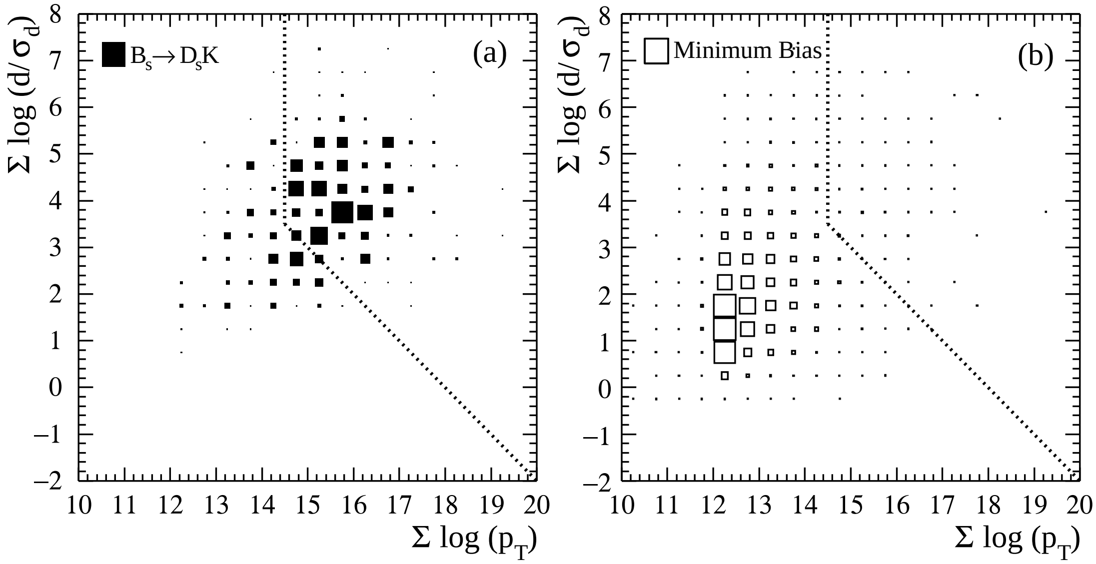

Figure 28: The logarithmic sum of the p_{T} of the two VELO–TT tracks with the largest p_{T} in the event versus the logarithmic sum of their impact parameter significance for (a) off-line selected $\mathrm{B_s^0} \to \mathrm{D_s^-K^+}$ events, and (b) minimum-bias events which have been accepted by L0. Indicated is the cut which selects 4% of the minimum-bias events.

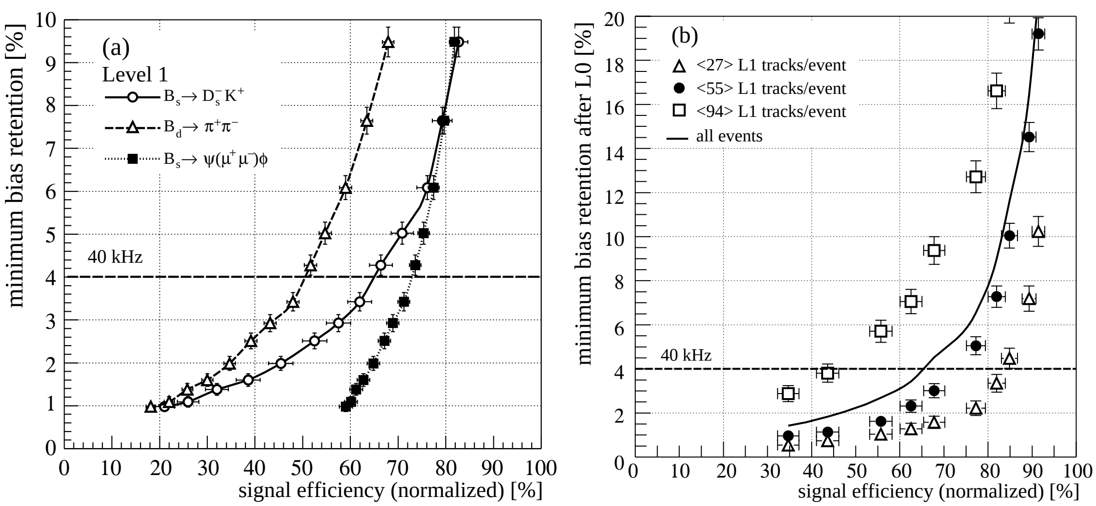

Figure 29: (a) The efficiency of L1 for a few off-line selected channels as a function of the L1 output rate. (b) The efficiency of L1 for off-line selected $\mathrm{B_s^0} \to \mathrm{D_s^{\mp}K^{\pm}}$ events as a function of the L1 output rate for subsamples with a different number of 2D tracks reconstructed. The average number of 2D tracks reconstructed in all minimum-bias events which are accepted by L0 is 58.

7 Physics Channel Reconstruction

In this section it is first shown, using as examples two different B decay modes, that the tracking performance of the reoptimized LHCb detector translates into vertex resolutions, proper-time resolutions and mass resolutions that are similar to those quoted in the TP [1], the VELO TDR [4] or the OT TDR [2]. Together with the fact that the particle-identification performance has changed little compared to the original design, this gives us confidence that the needed background rejection can be achieved in the offline selection. Our current estimates for total efficiencies and event yields are then presented, obtained on the basis of preliminary offline selections designed to reject the background, for the following channels: $\mathrm{B}^0 \to \pi^+\pi^-$, $\mathrm{K}^+\pi^-$, $\mathrm{K}^{*0}\gamma$, and $\mathrm{B}^0_\mathrm{s} \to \mathrm{K}^+\mathrm{K}^-$, $\mathrm{D}^-_\mathrm{s}\pi^+$, $\mathrm{D}^\mp_\mathrm{s}\mathrm{K}^\pm$, $\mathrm{J}/\psi\phi$.

The results presented here have been obtained with Monte Carlo events generated with tuned PYTHIA ($p_\mathrm{T}^\mathrm{min} = 3.47$ GeV/c for multi-parton interactions Model 3) and including the proper distribution for the number of simultaneous proton-proton interactions (see Section 2). These events have been fully simulated in the detector with GEANT, using a thorough description of the material foreseen in the experiment. The digitization part of the simulation took into account the details of the detector response, like inefficiencies, noise, cross-talk and spillover from previous and following bunch crossings (see Section 3). The input to any trigger or offline reconstruction algorithm was strictly limited to these digitized data. True Monte Carlo information was only used to assess resolutions and efficiencies, as the final step of performance monitoring.

7.1 Resolutions

The primary vertex resolution in the transverse directions (x and y) is currently found to be approximately 10 μm, in good agreement with the value quoted in the VELO TDR. Along the beam direction (z) a core sigma of 47 μm is obtained from a double Gaussian fit, to be compared to the VELO TDR resolution of 42 μm. However, the primary vertex algorithm is still being developed and should still improve, for example as it will be optimized for multiple-interaction events and modified to allow the tracks used to form a B candidate to be explicitly excluded from the fit.

The secondary and tertiary vertices have been determined using simple vertex fits, without mass or pointing constraints. Figure 30 shows the z resolutions for the D^-_s and B^0_s decay vertices obtained in the selection of the decay $\mathrm{B}^0_\mathrm{s} \to \mathrm{D}^-_\mathrm{s}\pi^+$ followed by $\mathrm{D}^-_\mathrm{s} \to \mathrm{K}^+\mathrm{K}^-\pi^-$. The core sigmas are 418 ± 31 μm (D^-_s) and 168 ± 15 μm (B^0_s), while the TP quotes a core resolution of 162 ± 9 μm in the latter case. The proper time of the B^0_s mesons reconstructed in this channel is shown in Fig. 31 (a) and has a core resolution of 42 ± 5 fs, dominated by the B^0_s vertex resolution, while a resolution of 43 fs was quoted in the TP. The proper time resolution for $\mathrm{B}^0 \to \pi^+\pi^-$ is similar, as shown in Fig. 31 (b) with $\sigma = 41 \pm 1$ fs from a single Gaussian fit, and is also consistent with the TP value.

Mass resolutions with the reoptimized detector are also found to be essentially unchanged from those quoted in previous TDRs [2, 4]. This is true for the $\mathrm{D}^-_\mathrm{s} \to \mathrm{K}^+\mathrm{K}^-\pi^-$

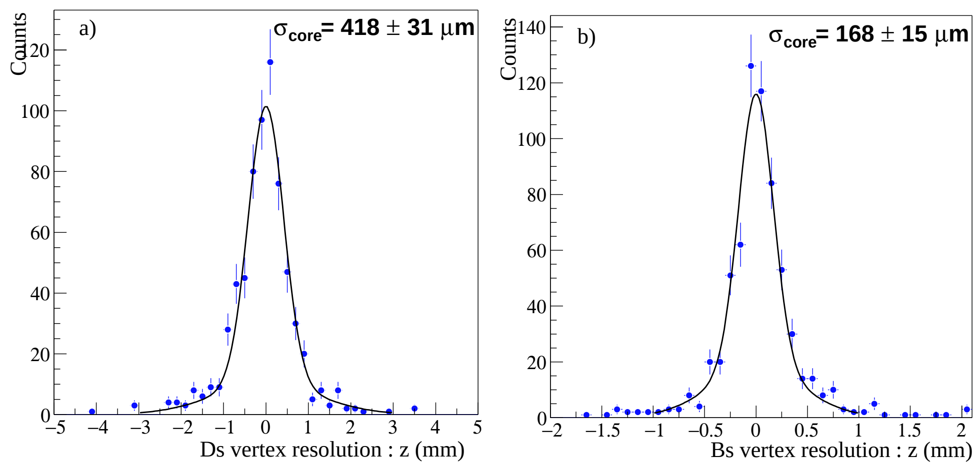

Figure 30: Vertex z resolution for reconstructed $\mathrm{B_s^0} \to \mathrm{D_s^-}\pi^+$, $\mathrm{D_s^-} \to \mathrm{K^+K^-}\pi^-$ decays: (a) $\mathrm{D_s^-}$ vertex, (b) $\mathrm{B_s^0}$ vertex.

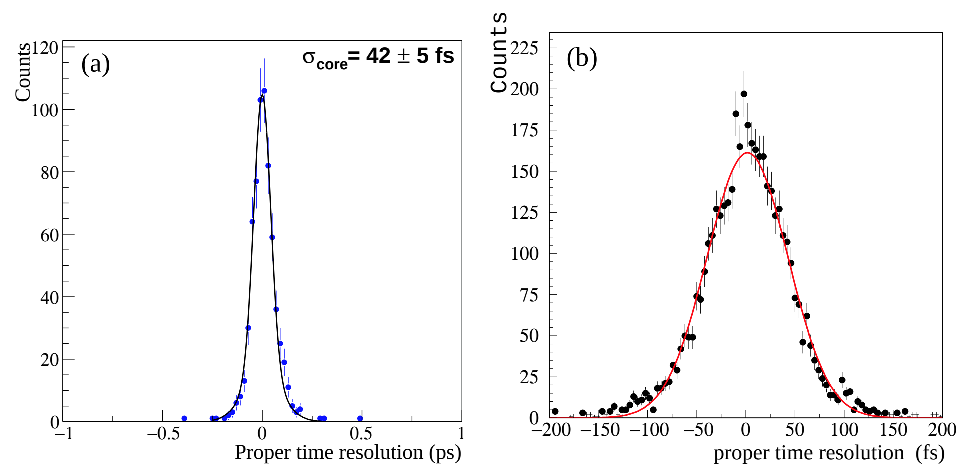

Figure 31: Proper-time resolution for (a) reconstructed $\mathrm{B_s^0} \to \mathrm{D_s^-}\pi^+$, (b) reconstructed $\mathrm{B^0} \to \pi^+\pi^-$ decays.

and $\mathrm{B_s^0} \to \mathrm{D_s^-}\pi^+$ mass resolutions shown in Fig. 32 (with core resolutions of $\sim$4 MeV/c^2 and $\sim$13 MeV/c^2), to which the track angular and momentum resolutions contribute with similar weights, as well as for the $\mathrm{B^0} \to \pi^+\pi^-$ mass resolution shown in Fig. 33 ($\sim$18 MeV/c^2), which is dominated by the momentum precision.

In general, the resolution plots now show some evidence of small non-Gaussian tails, as expected due to the improved realism since the time of the TP. These have not yet been investigated in detail, but it is seems reasonable that they are caused by pattern recognition mistakes (wrong hits on tracks) and by tracks suffering large multiple scattering (for example in the RF shield of the VELO which has a very non-uniform material distribution).

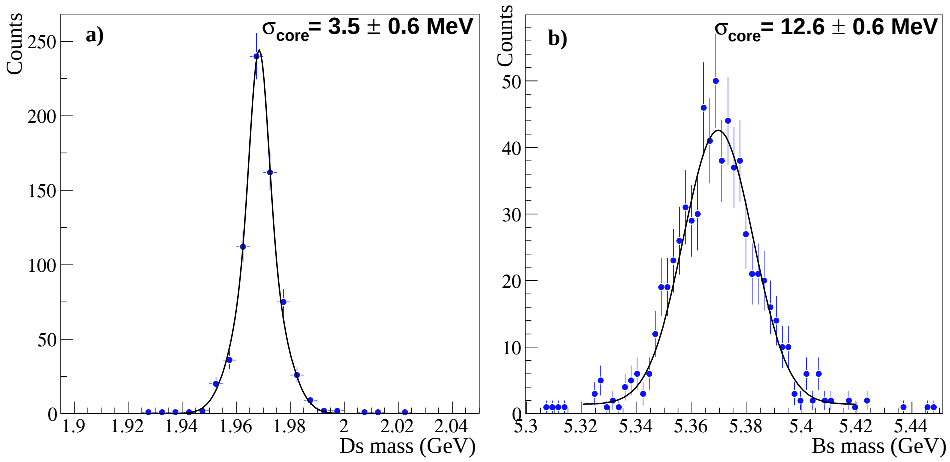

Figure 32: Mass resolution for (a) $D_s^- \to K^+K^-\pi^-$, (b) $B_s^0 \to D_s^-\pi^+$.

7.2 Background rejection

The rejection of physics background with the same topology as the signal is ensured by the quality of the particle identification and the mass resolutions. Figure 33 illustrates this for the $B^0 \to \pi^+\pi^-$, $B^0 \to K^+\pi^-$ and $B_s^0 \to K^+K^-$ selections, and shows, in each case, that the background from the other b-hadron decay modes to two charged tracks can be kept under control. The same conclusion is reached for the $B_s^0 \to D_s^-\pi^+$ background in the $B_s^0 \to D_s^\mp K^\pm$ selection, and for the $B^0 \to K^{*0}\pi^0$ background in the $B^0 \to K^{*0}\gamma$ selection.

Although sufficient background rejection power can already be demonstrated for these physics backgrounds, we are not yet in a position to prove it fully in the case of combinatorial background. Indeed such studies require more statistics than are available at present. Production of a sample of $\sim 10^7$ events is foreseen during Spring 2003, from which we will assess the background levels to be quoted in the forthcoming Reoptimization TDR. The signal efficiencies and event yields quoted here have been obtained with preliminary sets of offline and trigger selection cuts, which will be refined and optimized for the TDR. The present offline cuts have been chosen such as to reject all non-signal events in a sample of approximately 10^6 inclusive $b\bar{b}$ events, generated in the forward region of LHCb. Since this sample corresponds to about half a minute of data-taking at nominal LHCb luminosity, the upper limits that can be derived on the background efficiencies are still relatively loose. First encouraging attempts have been made to improve these limits by counting the background combinations in a relaxed B mass window. For example, in the case of the $B^0 \to \pi^+\pi^-$ selection, this limit can be reduced to match the background level that was quoted in the TP. In the present offline selections (which require minimum p and p_T values for the long tracks used to form B candidates), and within the limited statistics available, ghost tracks appear to contribute negligibly to the combinatorial background.

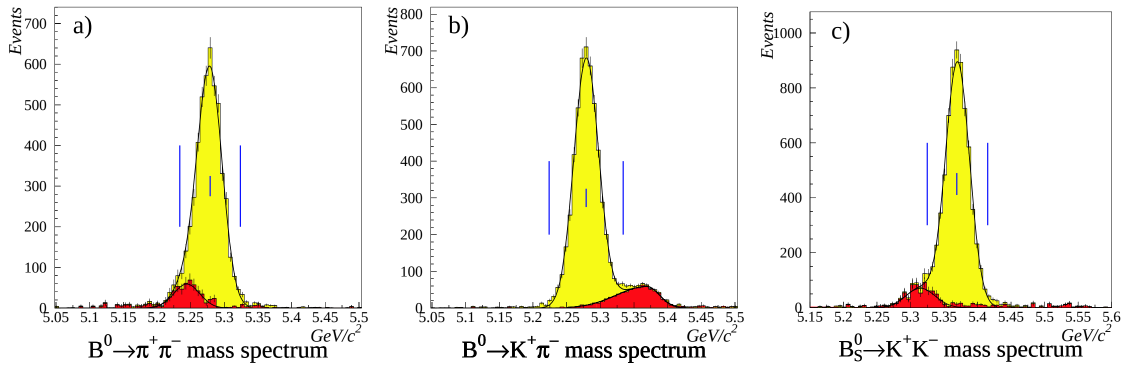

Figure 33: (a) $\mathrm{B}^0 \to \pi^+\pi^-$, (b) $\mathrm{B}^0 \to \mathrm{K}^+\pi^-$ and (c) $\mathrm{B}^0_\mathrm{s} \to \mathrm{K}^+\mathrm{K}^-$ mass spectra after selection cuts, including particle identification. In each plot, the light histogram shows the signal and the dark histogram shows the background from other b-hadron decays to two charged tracks, normalized assuming $\mathrm{BR}(\Lambda_\mathrm{b} \to \mathrm{p}\pi^-) = \mathrm{BR}(\mathrm{B}^0_\mathrm{s} \to \pi^+\mathrm{K}^-) = \mathrm{BR}(\mathrm{B}^0 \to \pi^+\pi^-)$, $\mathrm{BR}(\Lambda_\mathrm{b} \to \mathrm{pK}^-) = \mathrm{BR}(\mathrm{B}^0_\mathrm{s} \to \mathrm{K}^+\mathrm{K}^-) = \mathrm{BR}(\mathrm{B}^0 \to \mathrm{K}^+\pi^-)$, and using the measured values for $\mathrm{BR}(\mathrm{B}^0 \to \pi^+\pi^-)$, $\mathrm{BR}(\mathrm{B}^0 \to \mathrm{K}^+\pi^-)$ and the b-hadron production fractions [40].

7.3 Preliminary signal efficiencies and event yields

We present here results on the following physics channels: $\mathrm{B}^0 \to \pi^+\pi^-$, $\mathrm{B}^0 \to \mathrm{K}^+\pi^-$, $\mathrm{B}^0_\mathrm{s} \to \mathrm{K}^+\mathrm{K}^-$, $\mathrm{B}^0_\mathrm{s} \to \mathrm{D}^-_\mathrm{s}(\mathrm{K}^+\mathrm{K}^-\pi^-)\pi^+$, $\mathrm{B}^0_\mathrm{s} \to \mathrm{D}^\mp_\mathrm{s}(\mathrm{K}^\pm\mathrm{K}^\mp\pi^\mp)\mathrm{K}^\pm$, $\mathrm{B}^0_\mathrm{s} \to \mathrm{J}/\psi(\mu^+\mu^-)\phi(\mathrm{K}^+\mathrm{K}^-)$, $\mathrm{B}^0_\mathrm{s} \to \mathrm{J}/\psi(\mathrm{e}^+\mathrm{e}^-)\phi(\mathrm{K}^+\mathrm{K}^-)$, and $\mathrm{B}^0 \to \mathrm{K}^{*0}(\mathrm{K}^+\pi^-)\gamma$. The $\mathrm{D}^-_\mathrm{s} \to \mathrm{K}^+\mathrm{K}^-\pi^-$ decay is generated using 3-body phase space, without yet implementing intermediate resonances. For the generation of $\mathrm{J}/\psi \to \ell^+\ell^-$ decays, first-order QED radiative processes are included with a 1 MeV cut-off on the radiative photon. Spin and angular momentum is taken into account in the generation of the decay $\mathrm{B}^0 \to \mathrm{K}^{*0}(\mathrm{K}^+\pi^-)\gamma$.

The total signal efficiencies obtained in our present preliminary studies are given in the first column of Table 4. They are normalized to signal decays produced in the full 4π solid angle, in events generated with the expected pile-up as described in Section 2. Efficiencies of the high-level trigger and flavour tagging are not yet included. The total efficiency is given by various factors. For the $\mathrm{B}^0 \to \pi^+\pi^-$decay mode for example, it is a product of 13% geometrical acceptance, 96% track reconstruction efficiency per track, 22% efficiency for the offline selection, 61% for the Level-0 and 51% for the Level-1 trigger efficiencies.

The second column of Table 4 gives estimates for untagged event yields expected in 2 fb^{-1} of data, corresponding to a "nominal" year of $10^7\,\mathrm{s}$ at an average luminosity of $2 \times 10^{32}\ \mathrm{cm}^{-2}\mathrm{s}^{-1}$ with 25 ns bunch spacing. As in the TP, and as agreed amongst the LHC experiments at the time of the 1999 Workshop on LHC physics, a $\mathrm{b\bar{b}}$ production cross-section of 500 μb has been assumed for the yield calculations.[4] Whenever possible, the branching ratios involved (including the b-quark fragmenta-

[4]Given this assumption, our Monte Carlo trigger studies are somewhat conservative, as the minimum bias sample used contains 633 μb of $\mathrm{b\bar{b}}$ production.

Table 4: Current estimates for the total efficiencies and the untagged annual yields of interesting b-hadron decays, including their charge-conjugates, in events with any number of interactions. For comparison, the TP yields are also given, after adjustment to the same set of assumed branching ratios.

Channel (c.c. included)	efficiency	yield	TP
$B^0 \to \pi^+\pi^-$	0.78%	27k	11k
$B^0 \to K^+\pi^-$	0.85%	115k	38k
$B^0_s \to K^+K^-$	0.94%	35k	–
$B^0_s \to D^-_s\pi^+$	0.26%	72k	86k
$B^0_s \to D^\mp_s K^\pm$	0.34%	8k	6k
$B^0_s \to J/\psi(\mu^+\mu^-)\phi$	1.66%	109k	81k
$B^0_s \to J/\psi(e^+e^-)\phi$	0.29%	19k	32k
$B^0 \to K^{*0}\gamma$	0.09%	20k	22k

tion probabilities into B^0 and B^0_s mesons) are taken from the Particle Data Group [40]. The unmeasured $B^0_s \to K^+K^-$ decay is assumed to have the same branching ratio as $B^0 \to K^+\pi^-$ and the unmeasured $B^0_s \to D^\mp_s K^\pm$ branching ratios are assumed to sum up to 2.5×10^{-4}.

Since the time of the TP, many conditions and assumptions have changed. The most significant changes are that the current performance is based on a more realistic description of the LHC collisions, a more realistic detector description, and a new reconstruction software that does not use the Monte Carlo truth at any stage of the analysis. In addition, events with multiple interactions were ignored at the time of the TP (and the performance determined just with single-interaction events), while pileup is now treated in a proper way. Hence, the total efficencies of Table 4 do not have the same meaning as the ones quoted in the TP. We therefore compare the final yields, which are more representative of the physics potential of LHCb.

For the purpose of comparison, the last column of Table 4 reproduces the untagged yields from the TP, after adjustment to the present set of branching ratios. In general, the yields are expected to decrease due to the greater realism of the simulation and reconstruction, but this is compensated by improvements in the trigger and by accepting a fraction of events with multiple interactions. As can be seen from the table, the yields expected for the two-body hadronic modes are now substantially higher than those in the TP; this is due to improvements in the off-line selection. Trigger improvements are responsible for a larger yield in decays with a pair of muons. For the mode with electrons, there is currently a lower yield than in the TP, but work is still ongoing to optimize electron reconstruction. For the other modes considered in this report, the yields are comparable to the TP.

8 Conclusions

As a result of the effort that has been made to reduce the detector material, the tracking system configuration of the LHCb detector has been substantially modified, reducing the number of tracking stations by more than half. The reoptimized tracking setup consists of four stations, one in front of the magnet and three behind. The station in front of the magnet is made of silicon microstrip detectors, and the three other stations have an identical design to that presented in the Outer Tracker TDR, i.e. a combination of straw drift chambers and silicon microstrip detectors. The VELO is now used as an integral part of the tracking system. Detailed simulation studies show that the tracking efficiency for tracks traversing the whole tracking system is comparable to, if not better than, that obtained by a tracking system with nine tracking stations presented in the Outer Tracker TDR. The new tracking configuration is very robust and the efficiency would not be significantly affected even if the track multiplicity were higher than expected by a factor of two. There are ghost tracks, however at a low enough rate that they have no noticeable effect on the physics analyses.

By reconstructing various B decay final states and examining the invariant-mass and proper-time resolutions, we conclude that the quality of the reconstructed tracks has not deteriorated by reducing the number of tracking stations. Neither has the performance of the particle identification been affected. When similar performance can be achieved, a tracking system based on fewer tracking stations is advantageous. It contains less material, causing less multiple scattering and generating a smaller number of secondary particles due to photon conversions. Fewer particles are lost due to interacting strongly with material. The system is also simpler to maintain and operate, and the reduced event size simplifies the design of the higher level trigger and data acquision.

In addition to the reduction in number of the tracking stations, the reoptimized LHCb detector introduces magnetic field between VELO and the tracking station in front of the magnet, in order to enhance the performance and robustness of the trigger. Simulation study shows that the trigger efficiencies for interesting B decay modes indeed improve. The RICH-1 design is being modified in order to protect its photon detectors from the field.

The physics performance study also shows that the reoptimized LHCb detector will be able to reconstruct a similar statistics of B meson decays of interest as given in the Technical Proposal, and hence maintain its physics potential. However, for more complete studies, in particular the study of combinatorial background for the reconstructed B-meson signals, a large sample of events with inclusive $b\overline{b}$ decays is needed, and a production of $\sim$10 M events is planned for February 2003. Physics performance studied with those events, together with the revised designs of RICH-1 and the tracking station in front of the magnet, will be presented in the Technical Design Report for the reoptimized LHCb detector to be submitted in September 2003.

References

[1] S. Amato *et al.* (LHCb Collaboration), Technical Proposal, CERN–LHCC/1998–4.

[2] P.R. Barbosa *et al.* (LHCb Collaboration), Outer Tracker Technical Design Report, CERN–LHCC/2001–024.

[3] R. Hierck, M. Merk and M. Needham, *Particle interactions in the LHCb detector*, LHCb/2001–090.

[4] P.R. Barbosa *et al.* (LHCb Collaboration), Vertex Locator Technical Design Report, CERN–LHCC/2001–011.

[5] S. Amato *et al.* (LHCb Collaboration), RICH Technical Design Report, CERN–LHCC/2000–037.

[6] M. Needham, *Electron Reconstruction Studies*, LHCb/2001–102.

[7] S. Amato *et al.* (LHCb Collaboration), Muon System Technical Design Report, CERN–LHCC/2001–010.

[8] A. Franca Barbosa *et al.*, (LHCb Collaboration), Inner Tracker Technical Design Report, CERN–LHCC/2002–029.

[9] F. Fiedler, *Super Level-1*, LHCb/2002–012;
N. Tuning, *Tuning the Super Level-1 algorithm to the VELO TDR geometry*, LHCb/2002–028.

[10] H. Dijkstra *et al.*, *The use of the TT1 tracking station in the Level-1 trigger*, LHCb/2002–045.

[11] T. Sjöstrand *et al.*, Computer Physics Commun. **135** (2001) 238.

[12] T. Sjöstrand and M. van Zijl, *A multiple interaction model for the event structure in hadron collisions*, Phys. Rev. D **36** (1987) 2019.

[13] G.J. Alner *et al.*, UA5 collaboration, Phys. Reports **154** (1987) 247.

[14] F. Abe *et al.*, CDF collaboration, Phys. Rev. D **59** (1999) 32001.

[15] D. Acosta *et al.*, CDF collaboration, Phys. Rev. D **65** (2002) 072005.

[16] P. Bartalini *et al.*, LHCb/1999–028, contribution to the 1999 Workshop on Standard Model Physics (and more) at the LHC, CERN 2000–004, May 2000.

[17] G.J. Alner *et al.*, UA5 collaboration, Z. Phys. C **33** (1986) 1.

[18] F. Abe *et al.*, CDF collaboration, Phys. Rev. D **41** (1989) 2330.

[19] R. Field, private communication, and talks available at `http://www.phys.ufl.edu/~rfield/cdf/rdf_talks.html`;
we have considered the PYTHIA 6.2 settings referred to as "tune A" on `http://www.phys.ufl.edu/~rfield/cdf/tunes/rdf_tunes.html`.

[20] QQ program, `http://www.lns.cornell.edu/public/CLEO/soft/QQ`.

[21] GEANT Detector Description and Simulation Tool, CERN Program Library Long Write-up W5013 (1994).

[22] M. Needham, *Inner and Outer tracker occupancies in the Light LHCb detector*, LHCb/2002–032.

[23] A. Tsaregorodtsev, *Muon system parametrized background—algorithm and implementation*, LHCb/2000–011;
E. Aslanides *et al.*, *Performance of the muon trigger algorithm with the Muon TDR detector*, LHCb/2001–059.

[24] G. Barrand *et al.*, *GAUDI: a software architecture and framework for building HEP data processing applications*, Computer Physics Commun. **140** (2001) 45.

[25] *ROOT: an Object Oriented Analysis Framework*, `http://root.cern.ch`.

[26] A. Polouektov *et al.*, *First results from LHCb Inner Tracker performance studies using new digitization software*, LHCB/2001–118;
M. Needham, *New data model, digitization and reconstruction algorithms for the Inner Tracker*, LHCb/2002–030.

[27] M. Merk *et al.*, *An improved digitization procedure for the Outer Tracker*, LHCb/2001–055.

[28] R. Forty, *Track Seeding*, LHCb/2001–109.

[29] M. Benayoun and O. Callot, *The forward tracking, an optical model method*, LHCb/2002–008.

[30] J. van Tilburg, *Matching VELO tracks with seeding tracks*, LHCb/2001–103.

[31] R. Hierck *et al.*, *Performance of the LHCb OO track fitting software*, LHCb/2000–086.

[32] S. Amato *et al.* (LHCb Collaboration), Calorimeters Technical Design Report, CERN/LHCC 2000–036.

[33] R. Forty and O. Schneider, *RICH Pattern Recognition*, LHCb/1998–40.

[34] G. Wilkinson *et. al.*, *A simulation study of the LHCb RICH performance*, LHCb/2000–066.

[35] N. Brook *et. al.*, RICH-2 Engineering Design Report, LHCb/2002–009.

[36] E. Aslanides *et al.*, *A synchronous architecture for the L0 muon trigger*, LHCb/2001–010.

[37] O. Callot, *Performance of the calorimeter triggers*, LHCb/2000–050.

[38] N. van Bakel *et al.*, *The Beetle reference manual*, LHCb/2001–046.

[39] L. Wiggers, *Pile-up veto L0-trigger system for LHCb using large FPGA's*, 8th workshop on electronics for LHC experiments, Colmar, France, September 9–13, 2002.

[40] K. Hagiwara *et al.* (Particle Data Group), Phys. Rev. D **66** (2002) 010001.